1-1-2016

Principal Component Analysis-Based Anatomical Motion Models For Use In Adaptive Radiation Therapy Of Head And Neck Cancer Patients

Mikhail Aleksandrovich Chetvertkov
Wayne State University,

PRINCIPAL COMPONENT ANALYSIS-BASED ANATOMICAL MOTION MODELS FOR USE IN ADAPTIVE RADIATION THERAPY OF HEAD AND NECK CANCER PATIENTS

by

MIKHAIL A. CHETVERTKOV

DISSERTATION

Submitted to the Graduate School

of Wayne State University,

Detroit, Michigan

in partial fulfillment of the requirements

for the degree of

DOCTOR OF PHILOSOPHY

2016

MAJOR: MEDICAL PHYSICS

Approved By:

_____

Advisor Date

_____

_____

_____

_____

DEDICATION

To my mom, dad, sister, grandmother and grandfather and all my family in Russia whose support and love I could always feel even from overseas.

To my uncle, aunt and cousins for their help and support during my life in Detroit.

Finally, to my wife, Zhenya, for her endless love and support.

ACKNOWLEDGEMENTS

I would like to thank my dissertation committee: Dr. Indrin J. Chetty, Dr. Jay Burmeister, Dr. Michael Snyder, Dr. Joseph Rakowski, Dr. Stephen Brown, and in particular Dr. J. James Gordon for their help, support, constructive criticism and suggestions throughout this process.

I would also like to thank the ART H&N group members: Dr. Jinkoo Kim, Dr. Chang Liu, Dr. Akila Kumarasiri, Dr. Hualiang Zhong and Dr. Farzan Siddiqui for the many insightful discussions and thoughts during our meetings.

Henry Ford Health System holds research agreements with Philips healthcare, and this research was supported in part by a grant from Varian Medical Systems, Palo Alto, CA.

PREFACE

Note to the reader:

Chapter 1 defines the clinical problem and provides a brief introduction to conventional methods of handling geometric uncertainties inherent in the delivery of radiation for the treatment of cancer. Chapter 1 also presents the rationale of anatomical motion model development for improved radiation therapy outcomes.

Chapters 2-4 of this dissertation include patient-specific motion models based on standard and regularized Principal Component Analysis (PCA) approaches, and dosimetric outcomes that follow radiation treatments based on these models.

Finally, Chapter 5 presents conclusions and discussion of future directions.

TABLE OF CONTENTS

LIST OF TABLES

LIST OF FIGURES

LIST OF ABBREVIATIONS

3D ..... Three Dimensional

AAA ..... Analytical Anisotropic Algorithm

ART ..... Adaptive Radiation Therapy

CBCT ..... Cone-Beam CT

CF ..... Compression Factor

CT ..... Computed Tomography

CTV ..... Clinical Target Volume

DIR ..... Deformable Image Registration

DVF ..... Deformation Vector Field

DVH ..... Dose Volume Histogram

epCT ..... Estimated CT

EDVF ..... Eigen-DVF

GNU ..... GNU's Not Unix

GSL ..... GNU Scientific Library

GTV ..... Gross Tumor Volume

GU ..... Geometric Uncertainties

H&N ..... Head and Neck

HU ..... Hounsfield Units

ICRU ..... International Commission on Radiation Units

IGRT ..... Image-Guided Radiation Therapy

IMRT ..... Intensity Modulated Radiation Therapy

IRB ..... Institutional Review Board

Linac..... Linear Accelerator

NTCP ..... Normal Tissue Complication Probability

OAR ..... Organ-at-Risk

OSG ..... Organ Sample Generator

PC ..... Principal Component

PCA..... Principal Component Analysis

pCT ..... Planning CT

PRV..... Planning Risk Volume

PTV ..... Planning Target Volume

RAM ..... Random-Access Memory

QA..... Quality Assurance

QUANTEC..... Quantitative Analysis of Normal Tissue Effects in the Clinic

RPCA ..... Regularized Principal Component Analysis

SPCA ..... Standard Principal Component Analysis

TPS ..... Treatment Planning System

wCT..... Warped CT

CHAPTER 1 "INTRODUCTION"

Geometric Uncertainties in Radiation Therapy

Achieving tumor control with intensity modulated radiation therapy (IMRT) is both a geometric and a biological problem. The geometric aspect of the problem is to deliver a sufficient radiation dose to the tumor to sterilize it, while constraining dose to surrounding normal tissues to acceptable levels. The biological aspect of the problem is to understand issues such as dose-response relationships for tumors and normal tissues, the effect of different treatment regimens (e.g., hypofractionation), and the possible benefits of adjuvant chemotherapeutic agents. The biological aspect is not considered in this work.

In this work novel approaches to the geometric aspects of photon IMRT delivery to head and neck (H&N) were investigated – motion models of anatomical changes for H&N patients, to forecast anatomy and dose on future fractions, were constructed and tested.

The geometric problem may be summarized as follows. A physician delineates the gross tumor volume (GTV) and expands it by an appropriate margin to encompass expected microscopic disease. The resulting structure, the clinical target volume (CTV), is defined in the patient anatomical coordinate system (i.e., the coordinate system of the planning computed tomography (CT) image). If, in every treatment fraction, the patient could be aligned to the linear accelerator (linac) with perfect accuracy, allowing the linac isocenter to be located exactly at its intended position in the tumor, treatment could be planned and delivered to the CTV.

In reality, even when image guidance is used to carefully align the patient to the linac, the patient's intended position can still be offset from the isocenter[1]. Causes of offsets include: (i) setup errors[2] (imprecisions and inaccuracies inherent in the alignment tools used to position the patient with respect to the linac at the start of each fraction), and (ii) target (CTV) motion during delivery of each fraction[3, 4]. The above effects are random — target shape and position assume different random values, characterized by probability distributions, for each treatment course and fraction. Both effects create uncertainty in the position of the isocenter, and are accordingly referred to as geometric uncertainties (GUs).

Organ-at-risk (OAR) motion is a third category of GU[5]. At the start of a treatment fraction, an OAR can be offset from the isocenter by a different amount than in the planning CT (pCT), and can move relative to the isocenter (and CTV) during the fraction. The planning implications of OAR setup uncertainty and motion are different than for targets. One can reasonably hope to reduce target uncertainties through accurate (e.g., image-guided) setup. However, OAR motion is independent of the target, and cannot be eliminated through target alignment.

Delineation uncertainty is a fourth category of GU[6-8]. Delineation of gross tumor and organs-at-risk (OARs) on the planning CT is typically a manual operation subject to physician judgment. Errors or uncertainties can occur as a result of poor quality images, contouring shortcuts (such as contour interpolation across CT slices), time pressure on physicians, or unconscious bias when e.g., the physician is overly conservative when contouring targets in the vicinity of an OARs. Like setup uncertainties and tissue motion, delineation errors create a degree of geometric uncertainty in the true position of targets

and OARs with respect to the linac, and can therefore be addressed using the same planning techniques. Automated segmentation methods based on structure atlases[9] have the potential to reduce delineation uncertainties, but residual errors persist even with these methods.

Changes in patient anatomy during the course of radiation therapy (e.g. weight loss, tumor shrinkage, lymph node shrinkage, etc.) represent a fifth category of GU. One of the major reasons for such anatomical changes is the tissues' response to the radiation, causing e.g., tumor shrinkage, localized edema, etc. However, anatomical changes can occur for other reasons, e.g. general weight loss due to change in eating habits. Numerous research papers discuss importance of anatomical changes during radiation therapy[10-14].

The above five GUs should be considered during the treatment planning process in order to accurately perform radiation therapy.

Conventional Method of Handling Geometric Uncertainties

The conventional method of accounting for uncertainties in the position of the CTV relative to the linac (i.e., isocenter) is to expand the CTV to a planning target volume (PTV), and plan treatment to the PTV. Beams are configured, and IMRT inverse planning is performed, to ensure that in the static plan (i.e., the conventional plan generated prior to the start of treatment using the pCT image) the entire PTV receives the prescription dose (or a dose that is acceptably close to the prescription dose). In this case the PTV represents a bounding envelope within which one expects to find the entire CTV for every treatment fraction. This framework is described in ICRU reports 50 and 62[15, 16].

The size of the CTV-to-PTV margin controls the tradeoff between target and normal tissue doses. The margin needs to be large enough to ensure the CTV is covered most of the time, but not significantly larger, since that can result in OARs receiving unnecessary dose, leading to toxicity. The requirement that the CTV be covered (e.g., enclosed by the prescription dose isodose surface) "most of the time" is a coverage criterion. In the widely-used margin formula proposed by van Herk et al[17], "most of the time" is made mathematically precise by interpreting it to mean "95% minimum dose to CTV in 90% of patients". However, alternative approaches to PTV margins are possible. In clinical practice, margins are often set to round values such as 0.5 cm or 1.0 cm based on clinical conventions. In that case, the margin is justified by pointing to prior clinical experience that demonstrates generally acceptable treatment outcomes. There is a large number of published studies investigating appropriate CTV-to-PTV margin size for different treatment sites[18-21].

Conventional Method of Handling OAR Uncertainties

In considering geometric uncertainties, much of the published literature focuses on target coverage and CTV-to-PTV margins. The ICRU framework[15, 16] also allows for planning organ at risk volumes (PRVs) to be defined around OAR. The concept is similar to that of a PTV. The OAR-to-PRV margin is intended to create a 'buffer zone' around the OAR that can absorb geometric uncertainties. If OAR optimization criteria are applied to the PRV instead of the OAR, those constraints should be respected in the presence of geometric uncertainties.

However, practical application of PRVs is not straightforward. In the case of targets, there is generally a single prescription dose to be applied uniformly across the PTV. In that case, simple treatment models of the type used by van Herk et al.[22] can be used to estimate the amount by which the prescription dose isodose surface "pulls back" towards the CTV, as a result of the cumulative blurring of beams over multiple fractions. One can then compensate for this pull-back via the CTV-to-PTV margin.

For OARs there are typically multiple optimization criteria at different tolerance doses. The effect of blurring on the corresponding isodose surfaces will vary according to dose. For high doses, the isodose surface will pull back into the high dose region. For lower doses, it may push out from the high dose region, closer to the OARs. Based on the van Herk model, there is consequently no single OAR-to-PRV margin that will match all dose-volume criteria. Stroom and Heijmen[23] have investigated PRVs, concluding that they change the underlying OAR volume "in such a manner that dose-volume constraints stop making sense". For these reasons, PRVs are not widely used in clinical practice.

The non-use of PRVs means that the effects of geometric uncertainties (e.g., organ motion) on OAR are largely ignored. Failure to explicitly account for geometric uncertainties is thought to be one barrier to acquiring reliable and clinically useful biological outcomes models for OAR. The QUANTEC report[24] summarizes clinical data and models for a number of OAR. QUANTEC chapter 20[25] discusses the need to record "true dose" (i.e., dose delivered in the presence of geometric uncertainties) as opposed to planned dose, stating that "only careful studies that include estimates of (true dose) will allow us to confidently disentangle the effects of dosimetry and radiobiological sensitivity".

Conventional Method of Handling Delineation Uncertainties

In conventional clinical planning, delineation uncertainties are mostly ignored. One interpretation of current practice would be that delineation uncertainties are assumed to be sufficiently small that they are safely absorbed within current GTV-to-CTV and CTV-to-PTV margins, i.e., there is no need to explicitly account for them. However, the evidence from inter- and intra-observer studies[26-28] is that delineation uncertainties can be large relative to typical margins. Furthermore, as time goes on, advances in treatment delivery and imaging are reducing setup errors, and enabling organ motion to be quantitatively modeled more accurately than was previously possible. For these reasons, one can reasonably argue that delineation uncertainties need to be accurately quantified, and explicitly accounted for in treatment planning[7].

Role of Image-Guided Radiation Therapy and Adaptive Radiation Therapy in Handling Uncertainties

Image-guided radiation therapy (IGRT)[29] largely focuses on more accurate tumor targeting and tracking, and is less concerned with OAR motion. Recognizing that IGRT cannot mitigate the effects of changes in tumor shape, or motion of OAR with respect to the tumor, adaptive radiation therapy (ART)[30, 31] provides a complementary strategy in which the treatment plan is periodically updated throughout the treatment course. Both IGRT and ART have the goal of reducing geometric uncertainties. ART is likely to be most effective in cases where inter-fraction anatomic changes are significant with respect to intra-fraction changes. ART can be performed offline or online, with online planning being more effective, but more challenging due to the requirement to re-plan and perform quality assurance within a narrow time window.

Motivation for Motion Model Development in Radiation Therapy for Head and Neck Patients

IMRT in H&N cancer conforms very precisely to the three-dimensional (3D) shape of the tumor by modulating the intensity of the radiation beam in multiple small volumes. IMRT also allows higher radiation doses to be focused to regions within the tumor while minimizing the dose to surrounding normal critical structures[32-35]. Thus, the therapeutic index can potentially be increased by using IMRT as opposed to classical 3D conformal radiation therapy (RT).

However, conformal dose distributions are sensitive to GUs presented in patients, like daily setup errors or changes in the anatomy during treatment course due to the reasons mentioned above. For positional errors, online correction strategies like IGRT can help to minimize the effects of systematic and random setup errors[36-38]. However, residual setup uncertainties still exist and IGRT alone cannot compensate for non-rigid deformations of the anatomy[39].

ART is a potential solution for this problem. Although the concept of ART was proposed more than a decade ago[31], clinical implementation has lagged in part because of the inability to answer practical questions such as: What anatomical changes are important? How do we measure them? When to trigger re-planning? And how best to perform the re-planning?

Statement of the Problem

Having models of anatomical changes over the course of treatment is essential to answer the above questions. Models should take into account not only rigid body transformations but also deformations, and be capable of extracting useful information

about changes in patient anatomy, ideally early in the radiation therapy course.

Several mathematical models have been proposed to account for patient motion[40-46]. Among them, principal component analysis (PCA) was chosen in this study to model anatomical changes[47]. PCA is potentially a powerful and efficient method and is capable of identifying eigenmodes which are most responsible for the observed variations[48]. PCA compresses large multidimensional and unorganized data to a low-dimensional system of basis vectors (eigenvectors), representing major modes of anatomical change.

PCA models have been used for dosimetric evaluation of virtual prostate treatment courses[47], geometric coverage estimation[49], lung deformation modeling[50], automatic organ segmentation[51] and organ shape variability analysis[52]. However, to date, the implementation of PCA models has not been utilized for extracting systematic changes in patient anatomy during the H&N radiation therapy course. More information and material about PCA will be introduced in Chapter 2.

This work presents initial results on PCA modeling for characterizing systematic anatomical changes in H&N patients using daily cone-beam CT (CBCT) images. The goal is to reliably identify systematic anatomical changes early in the treatment course, in order to trigger re-planning decisions. A further goal is to capture normal tissue and tumor changes for treatment response assessment.

CHAPTER 2 "STANDARD PRINCIPAL COMPONENT ANALYSIS MODEL OF ANATOMICAL CHANGES IN HEAD AND NECK PATIENTS"

Introduction

The central idea of principal component analysis (PCA) is to reduce the dimensionality of a data set consisting of a large number of interrelated variables, while retaining as much as possible of the variation present in the data set[48]. To achieve this PCA performs orthonormal transformation of an original data set to a new set of variables called principal components (PC), which are orthonormal, and therefore uncorrelated to each other. The first PC is defined in such a way that it accounts for the largest possible variability in the data, while each succeeding PC in turn has the largest possible variability under the constraint that it is orthogonal to all preceding PCs.

PCA was first introduced in 1901 by K. Pearson[53]. Since then it became a handy tool which is used widely in predictive modeling.

This chapter discusses the develop of standard PCA (SPCA) models of anatomical change from daily CBCTs of H&N patients, and assesses the possibility of using these in adaptive radiation therapy and to extract quantitative information for treatment response assessment.

Materials and Methods

Clinical and Simulated Image Data

Ten H&N patients with daily CBCT imaging were retrospectively selected under an Institutional Review Board (IRB) approved protocol. Each patient experienced different systematic changes during the course of radiotherapy, like parotid shrinkage, weight loss,

tumor shrinkage in the oropharynx area, lymph node shrinkage in the left neck area, and base of tongue shrinkage. In Figure 2.1 patients which experienced such systematic changes are presented: parotid shrinkage (patient A), parotid shrinkage plus weight loss (patient B), tumor shrinkage in the oropharynx area (patient C) and lymph node shrinkage in the left neck area (patient D). Arrows indicate the region of change.

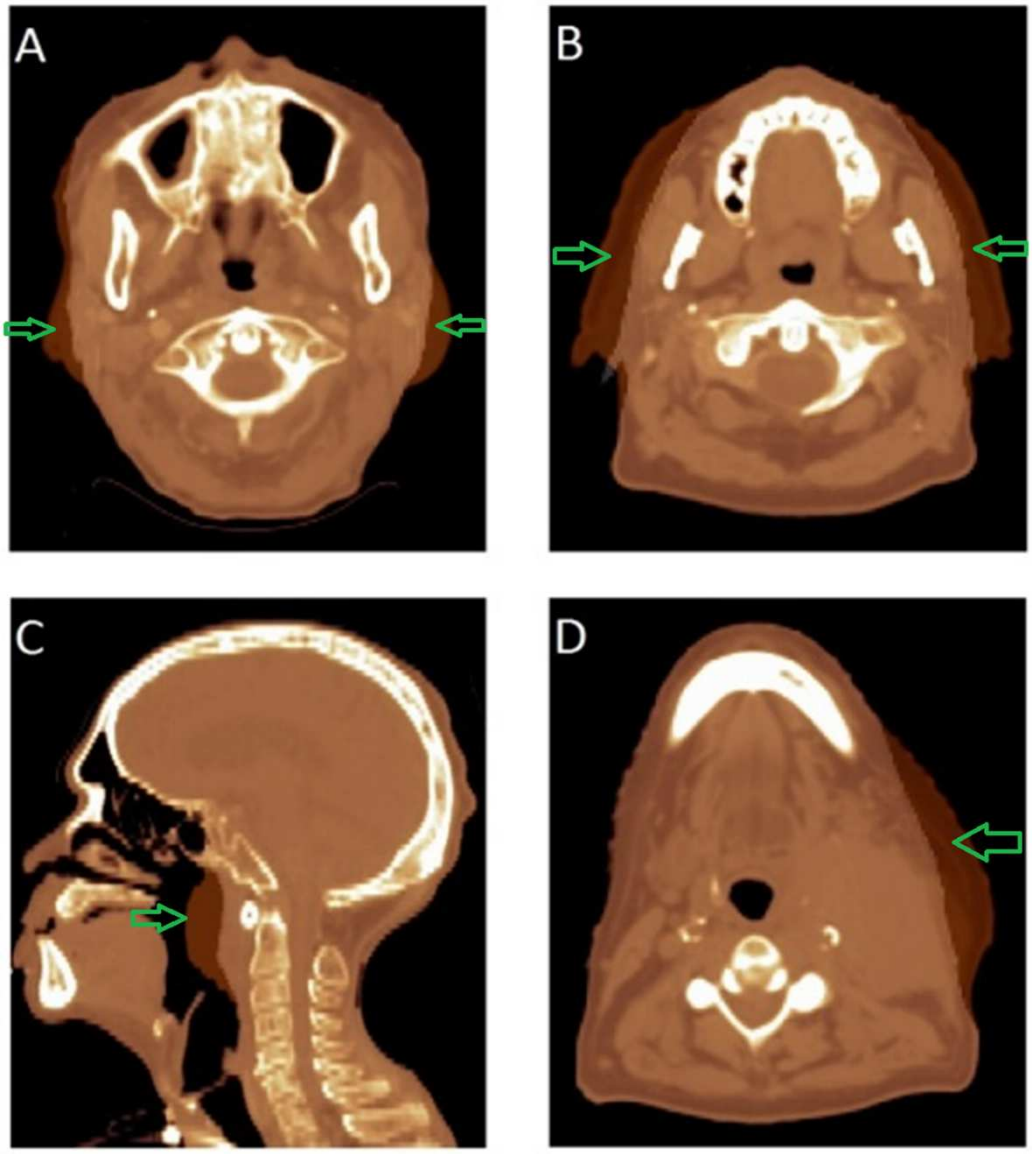

Figure 2.1 Blended pCT and wCT images of four (out of ten) patients; A - parotid gland shrinkage, B - parotid gland shrinkage and weight loss, C - Tumor shrinkage in the oropharynx, D - lymph node shrinkage in the left neck.

For each patient, a synthetic warped CT (wCT) was generated from the pCT image using an in-house developed interactive software tool. The interface of this tool is shown in Figure 2.2.

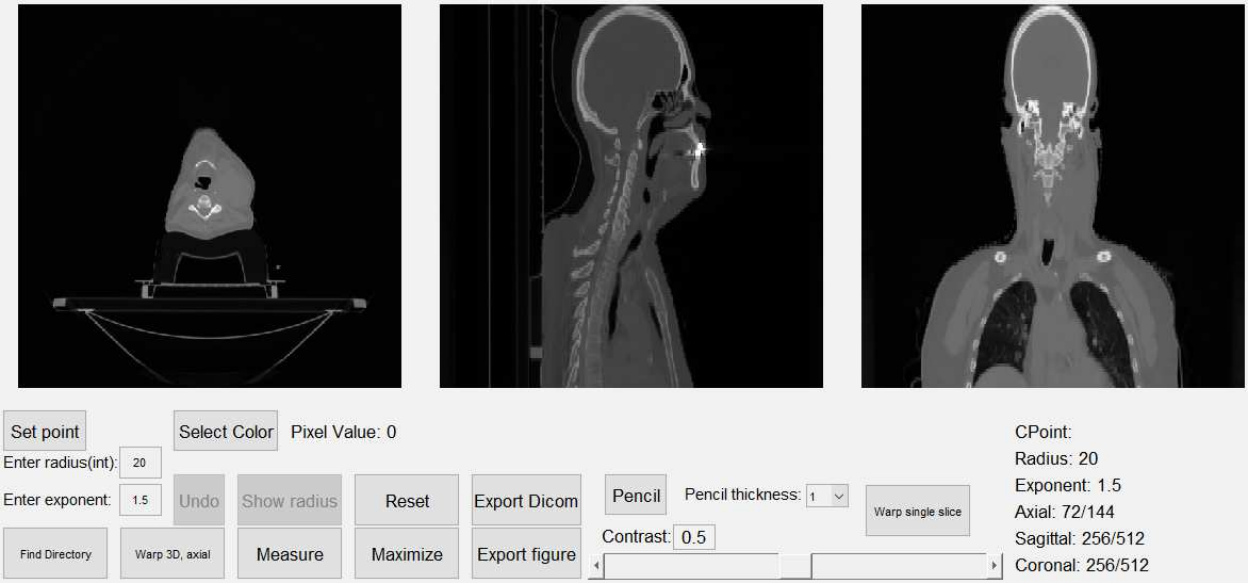

Figure 2.2 In-house developed interactive software tool (Matlab®) to perform warping of the images

The goal of the warping was to simulate the predominant localized systematic anatomical change over the duration of the patient treatment (Figure 2.1, arrows). So, for patient A, for example, the sole difference between the pCT and wCT was the deformation of the parotids and immediately adjacent tissue. Away from the parotids, the pCT and wCT matched exactly. The interactive warping tool was developed in Matlab® (MathWorks Inc., Natick, MA). It incorporated the barrel distortion function[54] and pencil tool, and allowed the user to iteratively expand, contract and shape a region of the pCT anatomy using a computer mouse. The generated wCTs were inspected by a radiation oncologist with expertise in H&N to ensure clinical realism.

The generated wCTs constitute digital phantoms, allowing PCA results to be evaluated in a controlled setting where the exact nature of anatomical change is known

a priori. Results below compare PCA's ability to extract anatomical change from digital phantoms (specifically, synthetic CBCTs generated from the wCT), as well as from real patients (i.e., clinical CBCTs). For clinical images, anatomical change is not known a priori and likely contains a variety of random components due to fraction-to-fraction setup uncertainties, posture variations, etc. Clinical images and deformation vector fields (DVFs) are therefore expected to be a greater challenge for the PCA technique.

Deformation Vector Fields Data

Prior to DVF generation, clinical or synthetic CBCT images were rigidly aligned with pCTs using bony skull and C2-C3 cervical vertebrae, to ensure all DVFs were relative to the fixed skull. The pCTs acted as reference imaged. DVFs were generated and manipulated in the Pinnacle® Treatment Planning System (TPS), utilizing Pinnacle plugins in conjunction with the open source GNU Scientific Library (GSL)[55] for matrix operations. DVFs for all patients were generated using Pinnacle's diffeomorphic demons algorithm[56-58]. A compression factor (CF) of 7 was used, meaning that a single DVF voxel covers 7 CT voxels (~ 7 mm) in the coronal and sagittal (X and Y) directions. This was done in order to keep PCA model generation numerically feasible. DVF voxel size in the axial (Z) direction was 3mm independent of the CF.

DVFs were restricted to a bounding box of the approximate size of the patient head and neck in order to speed up calculation. Bounding boxes were set sufficiently large to accommodate all anatomies. DVF values were set to zero for voxels outside the (pCT) patient body to avoid spurious deformations that are an artifact of the deformable image registration (DIR) algorithm. Given the number of voxels M, a DVF in 3D space is

represented as a vector of length 3M, representing X, Y and Z displacements.

It is worth noting the mathematical conventions that apply to DVFs. Each DVF is defined between a fixed image and a moving image. In the present case, the fixed image is the pCT, and the moving image is the wCT or CBCT. The DVF is defined on (i.e., is the same size as) the voxel grid in the fixed image. However, as explained by Yang[59], the DVF is a pull-back motion field. Each element of the DVF is a 3D vector (arrow) from a point in the fixed image to the matching point in the moving image. Consequently, one 'applies' the DVF to the moving image (wCT or CBCT) to recover the fixed image (pCT). In visual terms, given the moving image, one "pulls back" tissue volumes at arrow tips to the corresponding arrow bases, to recover the fixed image.

Clinical Deformation Vector Fields

In the following description a patient's i_{th} CBCT is denoted $CBCT_i$. Clinical DVFs were generated as follows:

$$D_{C,i} = DVF_{pCT \rightarrow CBCT_i}$$

$D_{C,i}$ denotes the clinical DVF from pCT to $CBCT_i$. It models systematic plus random change from planning to fraction *i*. The differential DVF, which models the motion difference between two successive fractions, is defined as follows:

$$DD_{C,i} = D_{C,i} - D_{C,i-1}$$

In the case of clinical images, the final available CBCT for the patient was regarded as the end-of-treatment anatomy (similar to the wCT).

Synthetic Deformation Vector Fields

Synthetic DVFs were generated using the following process:

$$D_W = DVF_{pCT \to wCT}$$

D_W denotes the DVF from pCT to synthetic wCT. It models systematic change from planning to end of treatment, based on the artificial deformation in the wCT. For a simulated treatment course of 35 fractions, let $D_{S,n}$ denote the systematic DVF (i.e., the DVF including only systematic change) from planning to the ith fraction, i = 1,...,35. Systematic DVFs were calculated using 3 different time models of patient response, linear, early and late:

$$D_{S,i} = D_W \left[\frac{i-1}{34}\right] \qquad \text{linear}$$

$$D_{S,i} = D_W \left[1 - \frac{1}{34^2}(35 - i)^2\right] \qquad \text{early}$$

$$D_{S,i} = D_W \left[\frac{1}{34^2}(i - 1)^2\right] \qquad \text{late}$$

In the above equations, the quantity in square brackets is the fraction of overall systematic change relative to the start of treatment. It ranges from zero in fraction 1 to one in fraction 35. This quantity is plotted in Figure 2.3. In the early (late) model, approximately 75% (25%) of change has occurred by the middle of treatment. These models are used to test PCA's ability to extract systematic motion from DVFs early in the treatment. For example, if PCA is asked to estimate systematic change from the first 5 treatment fractions, the late model presents PCA with much smaller systematic change (i.e., less information) from which to generate its model. The visual results of this test, averaged for SPCA and regularized PCA will be presented in the Results section of Chapter 3 to avoid repetitiveness in the Chapters, since this test showed almost identical behavior for both approaches.

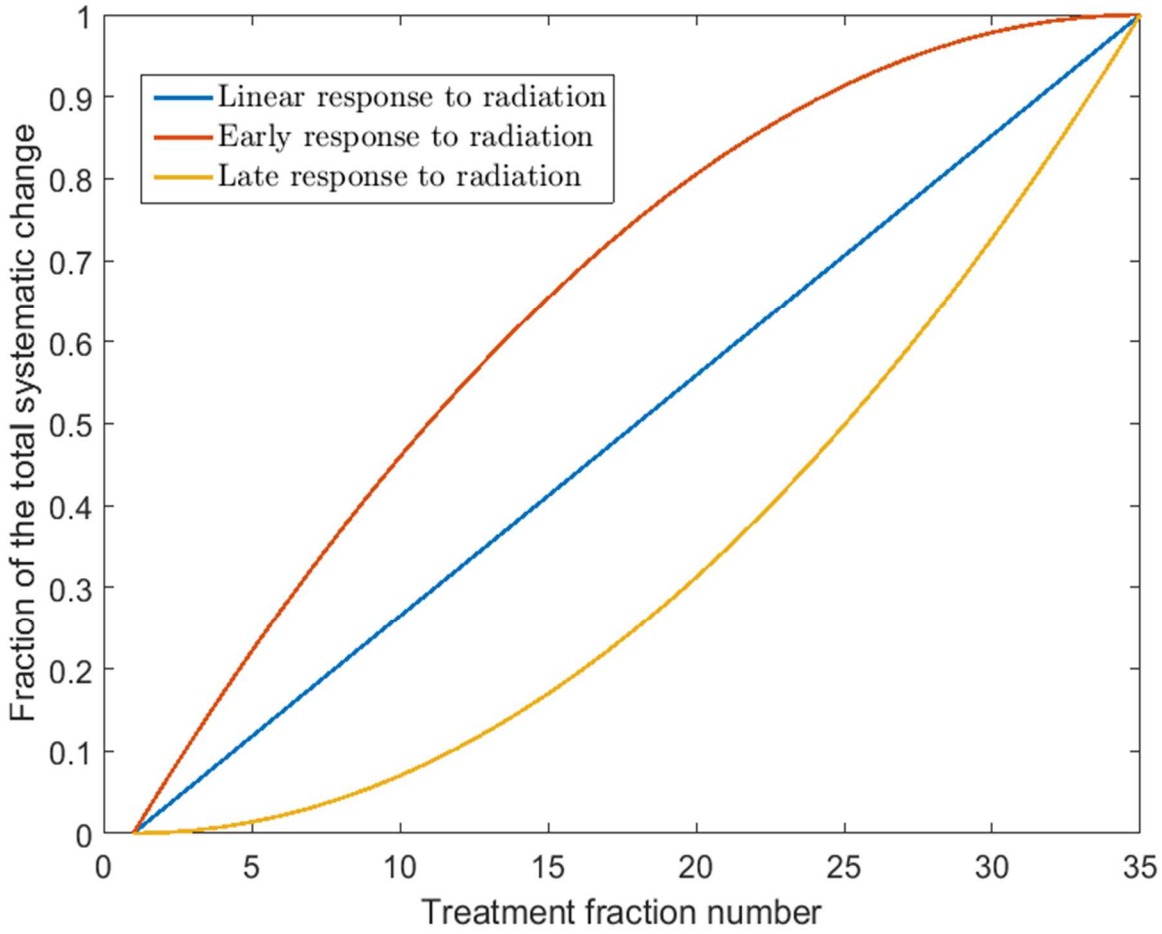

Figure 2.3 Early, linear and late models of patient response

Random changes were added to the synthetic DVFs as follows. Random DVFs D_R were modeled as scaled linear combinations of the $DD_{C,i}$: $D_R = \kappa \sum_i \alpha_i DD_{C,i}$, where $\alpha_i \epsilon [0,1]$ are uniformly distributed random weights summing to one, which vary from fraction to fraction, and κ is a scaling parameter taking the values 1, 3 or 5, that is fixed for each treatment course. The case $\kappa = 1$ approximates the magnitude of random motion present in clinical CBCTs. Cases $\kappa = 3 \ or \ 5$ artificially increase the magnitude of random motion, to test PCA's ability to extract systematic changes in the presence of increased random motion.

Finally, the synthetic DVF $D_{SR,i}$ for fraction i, incorporating both systematic and

random changes, was defined as follows:

$$D_{SR,n} = D_{S,n} + D_R = D_{S,n} + \kappa \sum_i \alpha_i DD_{C,i} \quad (2.1)$$

Note that D_R varies from fraction to fraction and between simulated treatment courses, as determined by the random number generator. In equation 2.1, the + symbol indicates element-by-element addition of DVFs.

PCA Models – Standard PCA

This section describes the generation of a patient-specific SPCA model. Let **D** = [D_1, ..., D_F] be an 3M x F matrix, whose column D_f is a DVF of length 3M, where M is the total number of voxels. In a clinical scenario, D_f is the DVF from the planning CT to the fraction *f* CBCT, *f* = 1, 2, ..., f ≤ N, where N is the number of fractions in the treatment course. Input data for PCA modeling is typically made zero-mean by first subtracting the mean DVF. Without loss of generality, we assume that the mean DVF $\overline{D}$ has already been subtracted from each of the D_f. DVFs from the first F fractions are used to build a model that can be used to predict anatomical changes for the remaining fractions. Let **E** = [E_1, ..., E_F] be an 3M x F matrix, whose columns E_f are eigenvectors, here referred as eigenDVFs (EDVFs). PCA solves the following constrained optimization problem for **E**:

$$\min_E \| \mathbf{D} - \mathbf{E}\mathbf{E}'\mathbf{D} \| \quad \text{subject to } \mathbf{E}'\mathbf{E} = \mathbf{I}_F \quad (2.2)$$

where $\mathbf{I}_F$ is the F x F identity matrix and, for arbitrary matrix $\mathbf{X} = [x_{ij}]$, ||·|| is the Frobenius norm: $\|\mathbf{X}\| = sqrt\left(\sum_{i,j} x_{ij}^2\right)$. The solution of equation 2.2 is a set of orthonormal EDVFs E_f, each of which is derived from an eigenvector of the covariance matrix $\mathbf{C} = \mathbf{D}'\mathbf{D}/\mathrm{M}$. The solution **E** can be obtained by using standard matrix operations to find the eigenvalues and eigenvectors of **C.** Further details about matrix operations used in this work to build

SPCA model are given in the Appendix. The resulting SPCA model is fully specified by the pair ($\bar{D}$,**E**). An arbitrary DVF *D* (3M x 1 column vector) may be expressed in matrix form

$$D = \bar{D} + \mathbf{E}w + \epsilon \quad (2.3)$$

where *w* is a (F x 1) column vector of EDVF weights w_j, and ϵ is an 3M x 1 column vector of errors ϵ_m. The error vector ϵ represents any variation present in *D* that is not expressible using a linear combination of the F EDVFs.

In the case of simulated treatment courses, SPCA models were generated from the first F = 5, 18 or 34 synthetic DVFs $D_{SR,i}$. These scenarios simulate the situation where a PCA model is generated after the first week of treatment (F=5), the first half of the 35-fraction course (F=18), and the complete course, except for the final fraction (F=34). In the case of clinical images, SPCA models were generated from the available 15 – 35 $D_{C,i}$, utilizing the initial 5, approximately half, and all but the final $D_{C,i}$.

Predictive Model

The magnitude of a PCA eigenvalue reflects the degree of variation in the DVF dataset that is contributed along the direction of the corresponding EDVF. EDVFs with the largest eigenvalues should account for the major modes of anatomical change. If PCA is successful, the expectation is that systematic components will be captured in the leading EDVFs. Random components will be captured in trailing EDVFs, or in the error vector ϵ in equation 2.3.

Once a PCA model has been generated using the first F DVFs, producing F EDVFs, one has the option of using a subset of K leading EDVFs (K ≤ F) to predict the

major mode of anatomical change for subsequent fractions. If, for example, there is only one major mode of anatomical change (e.g., tumor shrinkage), and that mode is captured in the first EDVF, then a satisfactory predictive model may be achieved using K = 1.

Additionally, the PCA modeling process makes no assumptions regarding how major modes of motion evolve during treatment. PCA EDVFs capture the direction but not the time-varying magnitude of anatomical changes. After generation of the PCA model, observed DVFs can be expressed as a linear combination of EDVFs (equation (2.3), where the weights w will in general vary as treatment progresses. The trajectory of weights w will indicate whether treatment response is early, linear or late, as in Fig. 2.3. The default predictive model given below makes the assumption that evolution is linear. However, this approach can be generalized to model early or late response, provided one has sufficient knowledge to justify those models.

The following step-wise procedure was adopted to build a linear predictive model:

M1. Using equation 2.3, estimate the weight vector $\hat{w}_f$ (F x 1 column vector of weights $\hat{w}_{f,j}$) corresponding to each of the input DVFs D_f from which the PCA model was generated: $\hat{w}_f = \left(D_f - \bar{D}\right)' \mathbf{E}$. Weight $\hat{w}_{f,j}$ for f = 1, ..., F represents the evolving contribution of EDVF E_j to anatomical change over fractions 1, ..., F.

M2. Separately for each value of j = 1, ..., F, perform a linear regression of weights $\hat{w}_{f,j}$ versus fraction number f. (For DVFs generated from clinical CBCTs, omit points for fractions where the CBCT is missing.) The intercept and slope of the linear fit to $\hat{w}_{f,j}$ are denoted by ρ_j and σ_j respectively.

M3. Estimate the DVF at fraction f, F < f ≤ N, by

$$\hat{D}_f = \bar{D} + \mathbf{E}_{\mathrm{K}} (\rho + \sigma \cdot f) \tag{2.4}$$

where ρ and σ are the K x 1 column vectors of ρ_j and σ_j, and $\mathbf{E}_K$ is the 3M x K matrix, whose columns E_j are the first K EDVFs.

The relationship between measured DVFs (i.e., input DVFs D_f in step M1) and predicted DVFs (output DVFs from equation 2.4) is illustrated in Figure 2.4. The orientation of DVF arrows is from fixed image to moving image, enabling CBCTs to be mapped to the pCT. In principle, these DVFs can be inverted to give DVFs that will map the pCT to predicted CBCTs for fractions F+1, ..., N. PCA-predicted DVFs are evaluated using criteria outlined in the next section.

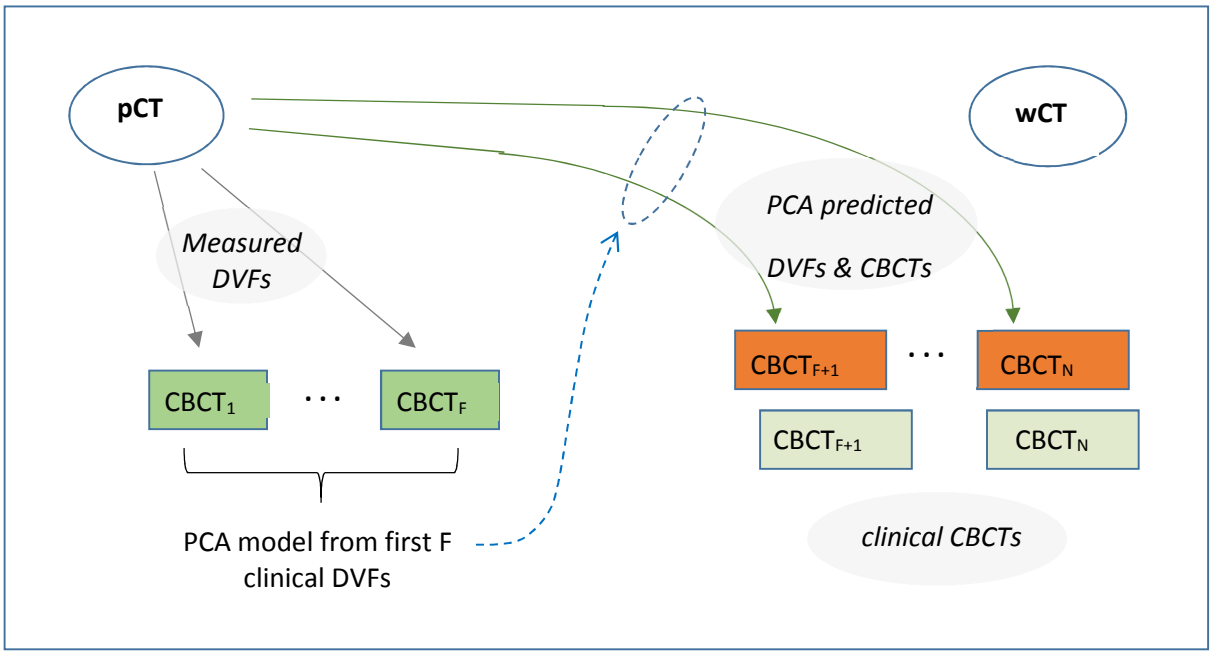

Figure 2.4 Relationship between measured and predicted DVFs

Model Evaluation

A hypothesis of this study is that the PCA model can successfully separate systematic from random anatomical changes, capturing systematic changes in a few leading EDVFs. One indicator of success is that, in step M2 above, the weights $\hat{w}_{f,j}$ associated with leading EDVFs exhibit non-zero slopes σ_j, high R^2 values and, more

generally, smooth and consistent evolution with fraction number *f*. Conversely, weights $\hat{w}_{f,j}$ associated with trailing EDVFs should exhibit near-zero slopes, low R^2, and purely random variation with fraction number *f*. A further qualitative indicator of PCA success is that the areas where leading EDVFs are non-zero are restricted to localized parts of the anatomy where systematic changes are occurring.

PCA models may also be evaluated quantitatively. This can be done by using the PCA model to warp the end-of-treatment anatomy to the predicted anatomy at the time of simulation. In this way one obtains an estimated planning CT, or epCT. Then one can compare epCT with the true planning CT (pCT) to assess how well the PCA model reproduces anatomical changes during treatment. The specific steps for generating epCT are:

S1. For simulated treatments, apply $\hat{D}_{35}$ from equation 2.4 to the wCT to get epCT.

S2. For clinical CBCT images, let f_E denote the fractions of the final CBCT image. Apply $\hat{D}_{f_E}$ from equation (4) to CBCT_{f_E} to get epCT.

Agreement between the pCT and epCT quantifies the difference between the real and estimated planning anatomies $\|\mathrm{pCT} - \mathrm{epCT}\|$. Note that the PCA model is intended to capture only systematic anatomical changes. The end-of-treatment anatomy, from which epCT is generated, will also incorporate random changes. Consequently, the difference metric $\|\mathrm{pCT} - \mathrm{epCT}\|$ will reflect how well PCA does at extracting the systematic component of anatomical change, but it will also reflect the effect of random anatomical changes not included in the model, and DIR uncertainties inherent in the DVFs used to construct the PCA model. Finally, in the case of the clinical CBCT images, epCT

is obtained by applying a modeled DVF to the end-of-treatment CBCT. Consequently, in this case epCT will include an increased level of noise inherent in CBCT (versus CT) images. This also will tend to increase the value of $\|\mathrm{pCT} - \mathrm{epCT}\|$.

We define images error vector E^F as the difference between pCT and epCT images:

$$E^F = pCT - epCT^F \qquad (2.5)$$

where $epCT^F$ is the estimated CT obtained from the PCA model that is generated from the first F fractions DVFs. E^F is a vector of length M. Each element of E^F is the error in the estimated CT number for the corresponding voxel.

For PCA models based on clinical CBCTs, where one is limited to the available CBCTs, we define the patient-specific distance metric to be the root mean square CT number difference:

$$\|pCT - eCT^F\| = \sqrt{\frac{1}{M}\sum_{k=1}^{M}(E^F)^2} \qquad (2.6)$$

For PCA models based on synthetic CBCT images generated from wCT, it is possible to perform S simulations, where each simulation generates a different realization of random changes throughout the treatment course. In this case we define the patient-specific distance metric to be the root mean square CT number difference, averaged over simulations:

$$\|pCT - eCT^F\| = \frac{1}{S}\sum_{s=1}^{S}\sqrt{\frac{1}{M}\sum_{k=1}^{M}(E^F)^2} \qquad (2.7)$$

In addition to these distance metrics, 3D gamma indices[60] were calculated between pCT and epCT images using 3% / 3mm criteria (3% difference in Hounsfield Units (HU), and 3mm distance-to-agreement). $\|\mathrm{pCT} - \mathrm{epCT}\|$ and gamma values were

calculated for PCA models generated using the first five fractions, half of the treatment fractions, and all but last treatment fraction.

Results

Qualitative Evaluation

Table 2.1 shows that for both simulated (linear, $\kappa = 1$) and clinical cases, the correlation coefficient R^2 of EDVF weights are significant only for the first EDVF — in Table 2.1, cases where $R^2 > 0.6$ are shaded.

		Simulated SPCA (linear) cases	Clinical cases
EDVF1	Fx_5	0.38 ± 0.34	0.24 ± 0.07
	Fx_half	0.82 ± 0.39	0.62 ± 0.19
	Fx_all_but_last	0.89 ± 0.14	0.65 ± 0.21
EDVF2	Fx_5	0.51 ± 0.32	0.01 ± 0.01
	Fx_half	0.03 ± 0.05	0.03 ± 0.04
	Fx_all_but_last	0.11 ± 0.20	0.01 ± 0.02
EDVF3	Fx_5	0.36 ± 0.34	0.21 ± 0.05
	Fx_half	0.14 ± 0.21	0.06 ± 0.08
	Fx_all_but_last	0.01 ± 0.02	0.04 ± 0.05
EDVF4	Fx_5	0.43 ± 0.30	0.10 ± 0.03
	Fx_half	0.05 ± 0.07	0.13 ± 0.08
	Fx_all_but_last	0.01±0.02	0.14 ± 0.19
EDVF5	Fx_5	0.38 ± 0.29	0.05 ± 0.07
	Fx_half	0.09 ± 0.10	0.07 ± 0.08
	Fx_all_but_last	0.01 ± 0.01	0.05 ± 0.01

Table 2.1 SPCA: R^2 correlation coefficient of performed linear regression of weights $\hat{w}_{f,j}$ versus fraction number *f*, averaged for all 10 patients (Step M2, Materials and Methods).

For EDVFs 2-5, R^2 coefficients are generally much lower. For simulated cases, R^2 values for EDVFs 2-5 in the 5-fraction PCA models (Fx_5) are higher (0.36 – 0.51). But those R^2 values drop substantially when more DVFs (fractions) are included in the PCA models, indicating that EDVFs 2-5 are not reliably capturing systematic changes. Based on Table 2.1, PCA models in this work utilize only one, or at most several, leading EDVFs.

For synthetic CBCTs, the estimated anatomy epCT at the time of simulation was reconstructed by applying $\widehat{D}_{35}$ (equation 2.4) to the wCT image. Figure 2.5 shows results for patient D, for whom PCA gave the best results (out of the 10 patients studied). Figure 2.6 shows results for patient A, for whom PCA gave the worst results. In each case, top panels show pCT (red) overlaid on the epCT (green). The left-most panel (A) is for a PCA

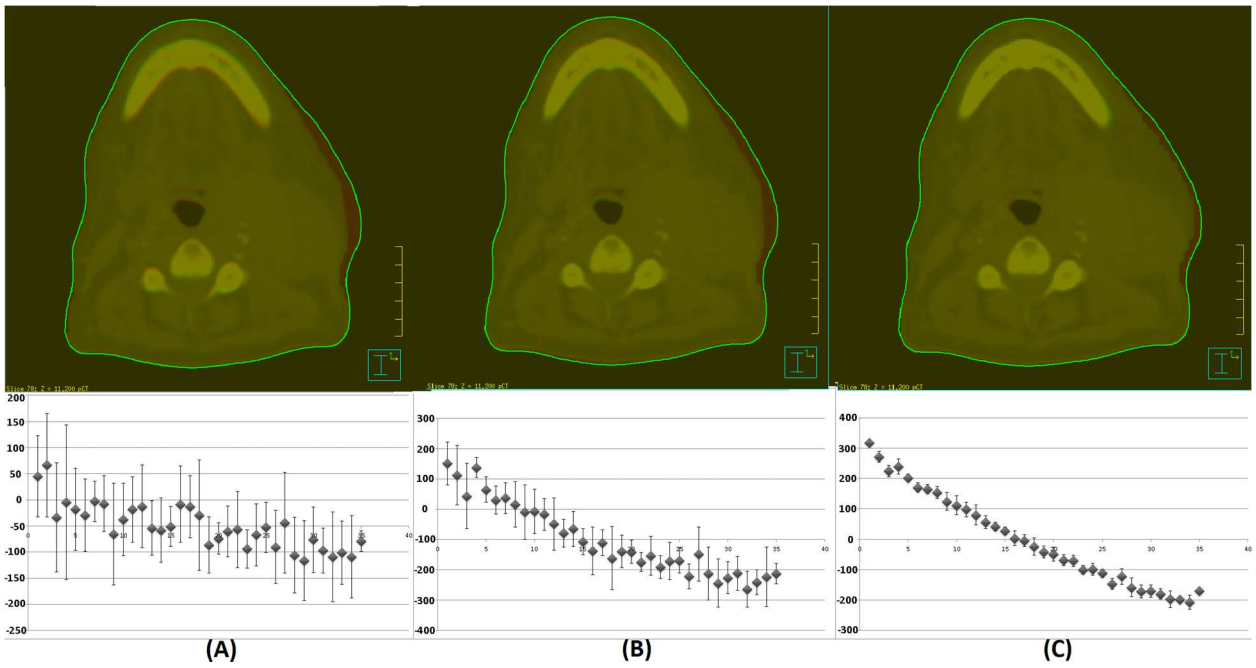

Figure 2.5 SPCA: Results of SPCA models generated from synthetic DVFs for patient D, for whom PCA modeling gave the best results

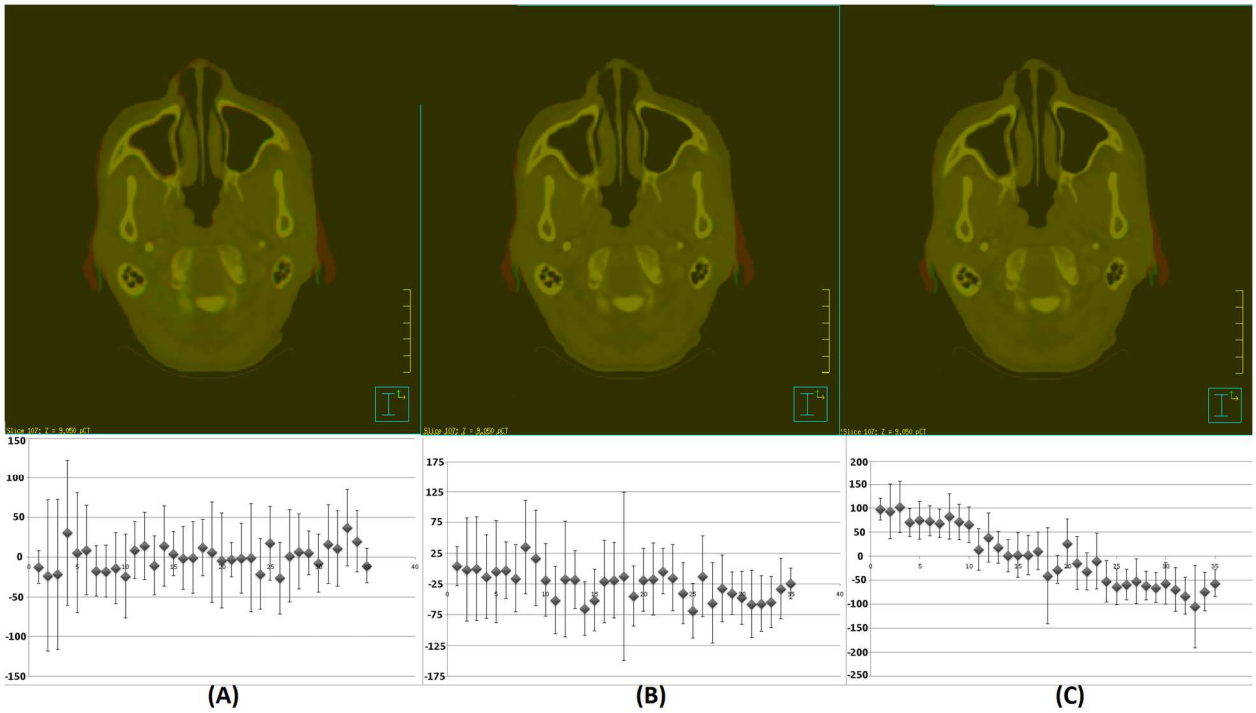

Figure 2.6 SPCA: Results of SPCA models generated from synthetic DVFs for patient A, for whom PCA modeling gave the worst results

model constructed from the first 5 treatment fractions. The middle panel (B) is for a PCA model constructed from the first 18 treatment fractions. The right-most panel (C) is for a PCA model constructed from all but the last treatment fraction. Lower panels in Figures 2.5 and 2.6 show the projections of all 35 simulated DVFs onto the leading EDVF. The error bars represent ± one standard deviation of EDVF weight values across simulated treatment courses having different random motion components. To generate these results, 10 different treatment courses were simulated for each patient.

Quantitative Evaluation

Figure 2.7 plots mean lengths of the image error vectors, $\|\mathrm{pCT} - \mathrm{epCT}\|$, equations (2.6) and (2.7), as a function of the number of fractions F from which the PCA model is generated: Patient A, PCA model generated from clinical CBCTs and DVFs; patient D,

PCA model generated from clinical CBCTs and DVFs; patient A, PCA model generated from synthetic wCT and DVFs; patient D, PCA model generated from synthetic wCT and DVFs.

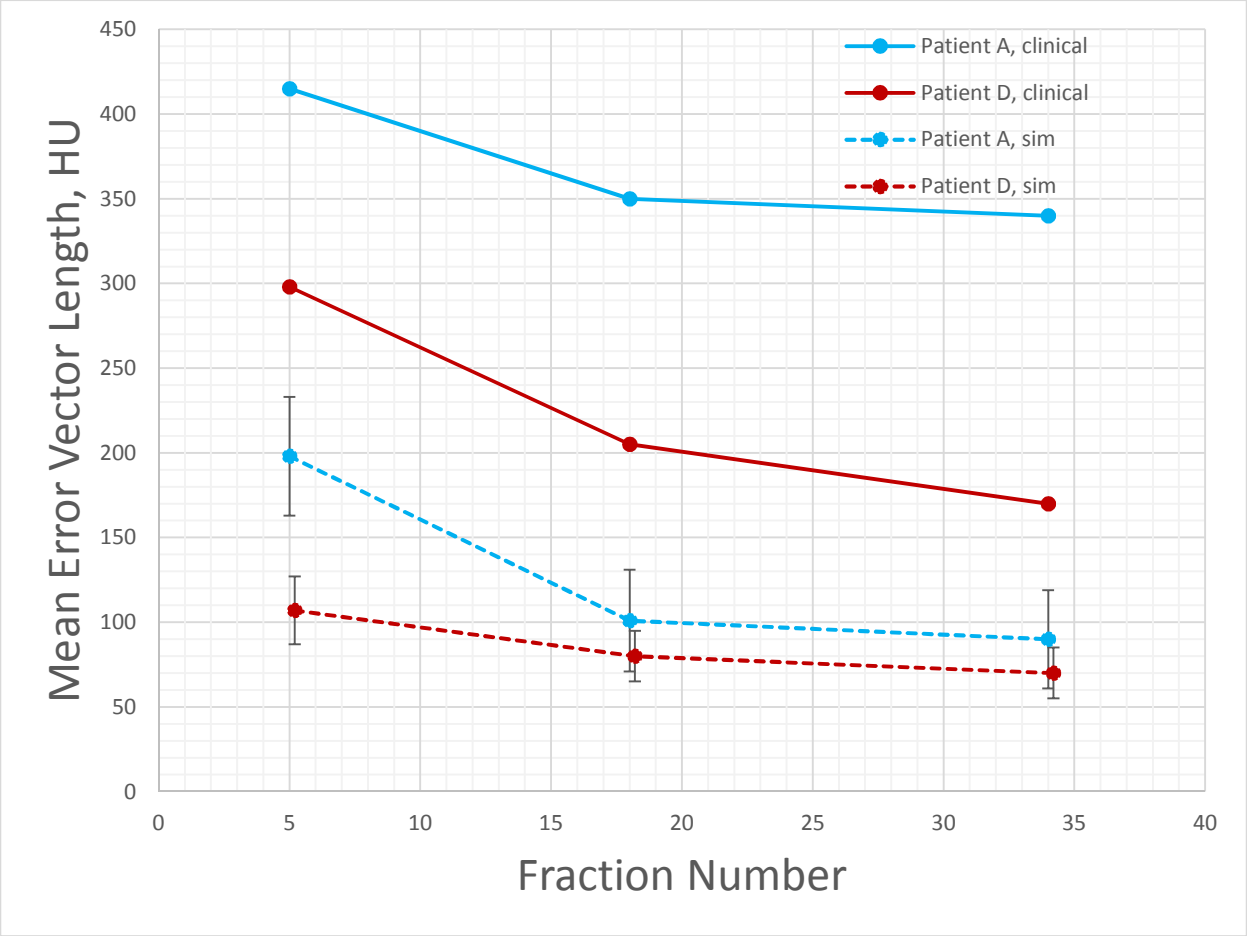

Figure 2.7 SPCA: Mean lengths of the image error as a function of the number of fractions F. Vector lengths are scaled by $1/\sqrt{M}$. Both the mean and standard deviation of the lengths of the image error vectors decrease as F increases

Although plotted against F = 5, 18, 34, clinical PCA models utilized the first 5 CBCTs, approximately half of available CBCTs, and all but the final CBCT. Vector lengths are scaled by $1/\sqrt{M}$ and plotted points are shifted slightly horizontally to avoid overlap of the error bars.

Table 2.2 shows results of gamma analysis of epCT versus pCT. Specifically, it shows the percentage of gamma values exceeding one, using 3%/3mm criteria for the

simulated and clinical cases of patients D (best case out of 10 patients) and patient A (worst case out of 10) for the SPCA models generated from first 5 fractions, half of the treatment fractions and all-but-last fraction.

		Patient D (best case out of 10 patients)	Patient A (worst case out of 10 patients)
Simulated	5 FX	0.25	0.50
	HALF	0.14	0.24
	ALL_BUT_LAST	0.11	0.18
Clinical	5 FX	2.39	4.15
	HALF	1.33	2.07
	ALL_BUT_LAST	1.15	2.02

Table 2.2 SPCA: Results of gamma analysis of epCT versus pCT: percent gamma values exceeding one, using 3%/3mm criteria

Discussion

Qualitative Evaluation

Table 2.1 shows that R^2 coefficients for the simulated linear cases for the first EDVF have values ~1, while for EDVFs 2-5 values are much less. This result shows that the leading first EDVF can capture the simulated linear major mode of anatomical change, while succeeding EDVFs capture residual errors and noise. The R^2 coefficient is a good metric to check if EDVFs captured the major anatomical change only if you expect these changes to be linear. This is not always the case during radiation therapy in real patients – changes could be non-linear and could appear early or late in the treatment.

But as stated in the Materials and Methods section above, the PCA modeling process makes no assumptions regarding how major modes of motion evolve during

treatment – it's just metric we use to evaluate it (like R^2 for the linear changes). PCA EDVFs capture the direction but not the magnitude of anatomical changes. Therefore, using proper metrics (i.e. splines or polynomials) it is possible to check if EDVFs captured major anatomical changes for non-linear cases. The results and discussion supporting this statement are presented in Chapter 3.

Figure 2.5 shows that, given the right conditions, SPCA modeling is capable of extracting the major mode of anatomical change during head and neck radiation therapy. The leading EDVF coefficients show a smooth progression during treatment, and the more CBCTs that are included in the SPCA model, the better the model becomes. This is indicated by a progressive tightening of the standard deviations of EDVF weights as one moves from model A (5 fractions), to model B (18 fractions), to model C (34 fractions).

In Figure 2.5 the modeled anatomical change, left neck lymph node shrinkage, is large — it affects a relatively large volume of the patient's anatomy. SPCA searches for EDVFs that can explain variability across CBCT images. If the modeled anatomical change is large, the SPCA technique is more easily able to 'extract' the major deformation mode(s) from noisy data. This explains why patient D has the best PCA model across the ten sampled patients.

In Figure 2.6 (patient A), the modeled anatomical change, bilateral parotid shrinkage, is relatively small — it affects a localized volume around the parotids. In this case SPCA finds it more difficult to isolate the anatomical change from other random variations that are present in the CBCT images. For this reason, the SPCA model is not as good as for patient D. The PCA models for F=5 and F=18 fractions show a fairly weak linear progression of the leading EDVF coefficient, and the standard deviation of the

coefficients is large, indicating that the SPCA technique is having a difficult time 'locking onto' the major deformation mode. Only when the treatment course is almost complete (column C, F=34) does the SPCA model become good enough to predict the anatomy, with a higher level of confidence.

One of the conclusions of this study is that SPCA — i.e., PCA applied directly to DVFs without any further enhancement or refinement — will find it difficult to extract smaller systematic anatomical changes from daily CBCT images. Where changes are small, SPCA will tend to be confused by other random motion present in the images, and the resulting PCA models will have diminished ability to predict or extrapolate anatomical changes.

Quantitative Evaluation

Figure 2.7 shows that larger HU errors occur for the SPCA models generated from clinical CBCTs (lines (a) and (b)), than those generated from synthetic images and DVFs (lines (c) and (d)). Synthetic DVFs were generated artificially by inserting one known anatomical change into the planning CT. Regions of the patient anatomy that were not affected by the change were identical throughout the treatment course, except for added random changes. This represents a best-case scenario for SPCA modeling. Having only one systematic change present in the images makes it easier for the SPCA method to capture that change within the leading EDVF.

Clinical CBCTs may include several types of systematic anatomical change — for example, lymph node shrinkage in conjunction with weight loss. Clinical CBCTs can also include random motion of the anatomy outside of the region directly involved in the

systematic change. Finally, evolution of the systematic change in clinical CBCTs may not follow a simple linear progression, as was the case with the synthetic DVFs. For these reasons, SPCA finds it more difficult to extract useful models from clinical CBCT images.

This conclusion is reinforced by the gamma results in Table 2.2. Those results show that the number of voxels in epCT that disagree with pCT by more than 3% or 3 mm is fairly modest for the SPCA models generated from synthetic DVFs, but much larger in models generated from clinical CBCTs.

Quantitative results shown in Figure 2.7 and Table 2.2 may be used as an indirect way of testing the accuracy of DVFs, or the accuracy of the reconstructed epCT (acquired by applying the last-fraction DVF from equation 2.4 to the pCT image) versus the pCT image. Although thorough testing of DVFs accuracy was out of the scope of this work, results of the quantitative analysis give an idea of how the number of fractions used to build a model and random changes presented in simulated and clinical data affect the quality of the last-fraction DVF and overall accuracy of the epCT with respect to the pCT image.

Within this work we evaluated whether SPCA models generated from clinical CBCTs could potentially be improved by including more than one leading EDVF. That is, using $K \geq 2$ as explained in the Predictive Model section above. However, for clinical SPCA models the R^2 coefficient was moderately good for the leading EDVF, but quite poor for EDVFs 2-5 (see Table 2.1), indicating that there was no improvement derived by including any EDVFs beyond the first. The conclusion of this work is that, particularly for smaller anatomical changes, SPCA becomes 'confused' by the variety of deformations and noise in clinical CBCT images, and therefore fails to extract major modes of

systematic change that are known to be present. In order to successfully model anatomical change in clinical CBCT images, the basic SPCA technique will need to be refined.

In Chapter 3 more extensive discussion about SPCA model and its comparison to more advanced regularized PCA (RPCA) model will be presented.

Conclusion

For the H&N patients treated with external beam radiation therapy, a SPCA model is a potential tool to identify patient anatomy changes early in the treatment course, and to make educated adaptive re-planning decisions. This study used synthetic (but realistic) DVFs, as well as clinical CBCTs, to evaluate the ability of the SPCA method to extract useful models of anatomical change. In particular, a primary goal of this work was to evaluate the ability of SPCA to separate systematic from random changes present in CBCT images.

The study shows that under the right conditions, SPCA can capture the major mode of systematic anatomical deformation in the leading EDVF. However, SPCA is most successful at identifying large changes (e.g., significant lymph node shrinkage), and less successful at identifying small changes (e.g., smaller changes in parotid glands). Additionally, SPCA is challenged by the variety of deformations and noise in clinical CBCT images, and therefore fails to extract major modes of systematic change that are known to be present. In order to successfully model anatomical change in clinical CBCT images, the basic SPCA technique will be refined using the regularized approach described in Chapter 3.

CHAPTER 3 "REGULARIZED PRINCIPAL COMPONENT ANALYSIS MODEL OF ANATOMICAL CHANGES IN HEAD AND NECK PATIENTS"

Introduction

The purpose of this Chapter is to reveal, building on the Materials and Methods section presented in Chapter 2, the details of developing regularized PCA (RPCA) models of anatomical changes from daily CBCTs images of H&N patients, and assess their potential use in ART, and for extracting quantitative information for treatment response assessment.

The general motivation to build the RPCA model is the same as for the SPCA (i.e., modeling of anatomical change, see the Introduction section in Chapter 2). The specific motivation is to improve on the SPCA results given in Chapter 2.

Materials and Methods

The dataset, DVFs and predictive model used to build the RPCA model are the same as described in Chapter 2. The difference is in the constraint optimization problem (equation 2, Chapter 2) one needs to solve to get EDVFs.

PCA Models – Regularized PCA

For reasons discussed below, standard PCA (SPCA) can produce EDVFs that are noisy and not physically meaningful. RPCA offers a solution for this problem. The method of generation of a patient-specific regularized RPCA model is similar to the SPCA model described earlier. The difference lies in the constrained optimization problem for **E** that PCA needs to solve for the regularized PCA approach**:**

$$\min_{E}\{\ \|\mathbf{D}-\mathbf{E}\mathbf{E}'\mathbf{D}\ \|^2+\tau_1\sum_{k=1}^{F}J(e_k)+\tau_2\sum_{k=1}^{F}\sum_{j=1}^{3M}e_k(s_j)\ \} \tag{3.1}$$

$$\text{subject to } \mathbf{E}'\mathbf{E}=\mathbf{I}_{\mathrm{F}}$$

where $\mathbf{I}_{\mathrm{F}}$ is the F x F identity matrix, $s_j=(x_j,y_j,z_j)'$, $\tau_1\geq 0$ is a smoothness parameter and the corresponding term $J(e_k)$ is a roughness penalty designed to enhance smoothness of EDVFs e_k, $\tau_2\geq 0$ is a sparseness parameter and the corresponding term is the L_1 Lasso penalty designed to promote sparse patterns in EDVFs by shrinking some principal component loadings to zero. The explanation of the methods used to solve the constrained optimization problem for sparse data sets could be found in Wang and Huang[61].

RPCA models are dependent on the choices of smoothing parameter τ_1 and sparseness parameter τ_2. Both parameters were empirically chosen with the assumption in mind that DVFs are intrinsically smooth, so the smoothness parameter was chosen to be less significant than the sparseness parameter. After experimentation, the following rules were adopted to set τ_1 and τ_2: $\tau_1=\frac{3M*F}{1000}$ and $\tau_2=\frac{3M*F}{100}$.

As before, the resulting PCA model is fully specified by the pair ($\bar{D}$, **E**), and an arbitrary DVF may be again expressed using equation 2.3. As for SPCA, RPCA models were generated from the first F = 5, 18 or 34 synthetic DVFs $D_{SR,i}$. In the case of clinical images, RPCA models were generated from the available 15 – 35 $D_{C,i}$, utilizing the initial 5, approximately half, and all but the final $D_{C,i}$.

Results

Qualitative Evaluation

Table 3.1 shows that for both simulated (linear, $\kappa=1$) and clinical cases, the

correlation coefficient R^2 of EDVF weights are significant only for the first EDVF — in Table 3.1, cases where $R^2 > 0.6$ are shaded.

For EDVFs 2-5, R^2 coefficients are generally much lower. For simulated cases, R^2 values for EDVFs 2-5 in the 5-fraction RPCA models (Fx_5) are higher (0.16 – 0.39). But those R^2 values drop substantially when more DVFs (fractions) are included in the RPCA models, indicating that EDVFs 2-5 are not reliably capturing systematic changes.

		Simulated RPCA (linear) cases	**Clinical cases**
EDVF1	Fx_5	0.57 ± 0.24	0.54 ± 0.21
	Fx_half	0.87 ± 0.19	0.77 ± 0.22
	Fx_all_but_last	0.94 ± 0.19	0.81 ± 0.18
EDVF2	Fx_5	0.39 ± 0.13	0.27 ± 0.10
	Fx_half	0.14 ± 0.05	0.11 ± 0.05
	Fx_all_but_last	0.21 ± 0.11	0.29 ± 0.05
EDVF3	Fx_5	0.16 ± 0.27	0.10 ± 0.05
	Fx_half	0.15 ± 0.22	0.15 ± 0.17
	Fx_all_but_last	0.07 ± 0.19	0.12 ± 0.12
EDVF4	Fx_5	0.27 ± 0.20	0.14 ± 0.09
	Fx_half	0.32 ± 0.11	0.20 ± 0.18
	Fx_all_but_last	0.10±0.12	0.12 ± 0.06
EDVF5	Fx_5	0.30 ± 0.17	0.04 ± 0.09
	Fx_half	0.12 ± 0.11	0.09 ± 0.11
	Fx_all_but_last	0.04 ± 0.07	0.09 ± 0.15

Table 3.1 RPCA: R^2 correlation coefficient of performed linear regression of weights $\hat{w}_{f,j}$ versus fraction number *f*, averaged for all 10 patients (Chapter 2, Step M2, Materials and Methods).

The estimated anatomy epCT at the time of simulation was reconstructed by applying $\widehat{D}_{35}$ (equation 2.4) to the wCT image. Figures 3.1 and 3.2 show result for the same patients as for SPCA model. Figure 3.1 shows results for the patient D, for whom RPCA gave the best results (out of the 10 patients studied). Figure 3.2 shows results for patient A, for whom RPCA gave the worst results. In each case, top panels show pCT (red) overlaid on the epCT (green). The left-most panel (A) is for a RPCA model constructed from the first 5 treatment fractions. The middle panel (B) is for a RPCA model constructed from the first 18 treatment fractions. The right-most panel (C) is for a RPCA model constructed from all but the last treatment fraction. Lower panels in Figures 3.1 and 3.2 show the projections of all 35 simulated DVFs onto the leading EDVF. The error bars represent ± one standard deviation of EDVF weight values across simulated treatment courses having different random motion components. To generate these results, 10 different treatment courses were simulated for each patient.

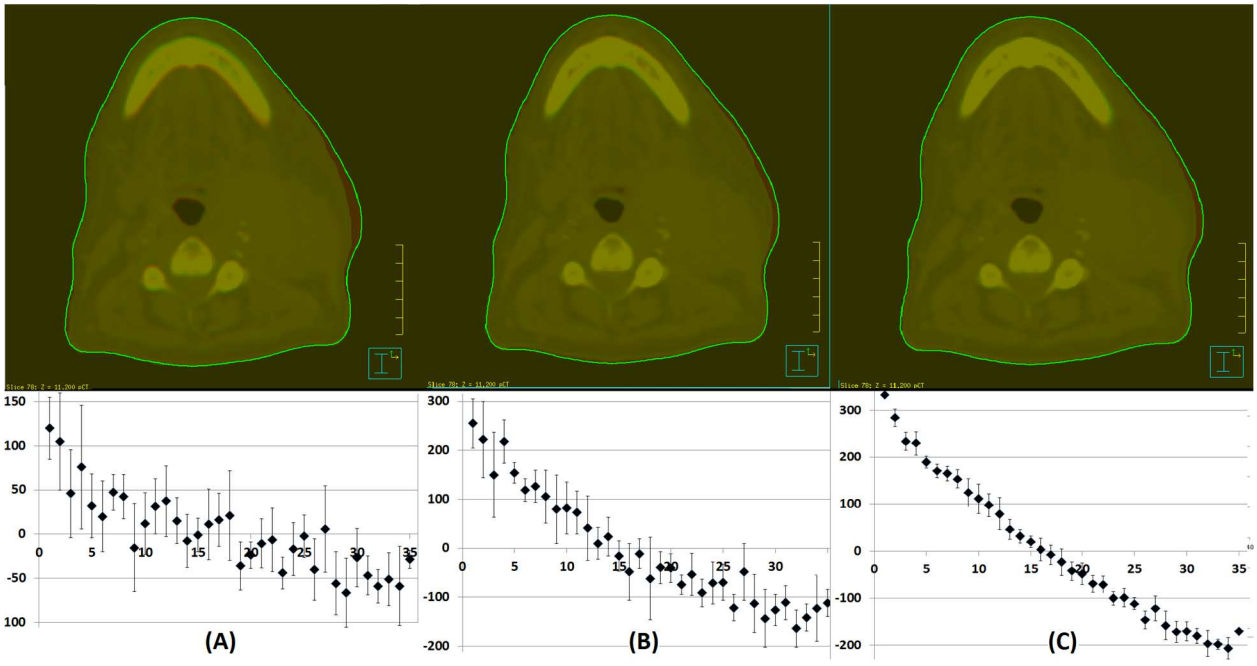

Figure 3.1 RPCA: Results of RPCA models generated from synthetic DVFs for patient D, for whom PCA modeling gave the best results

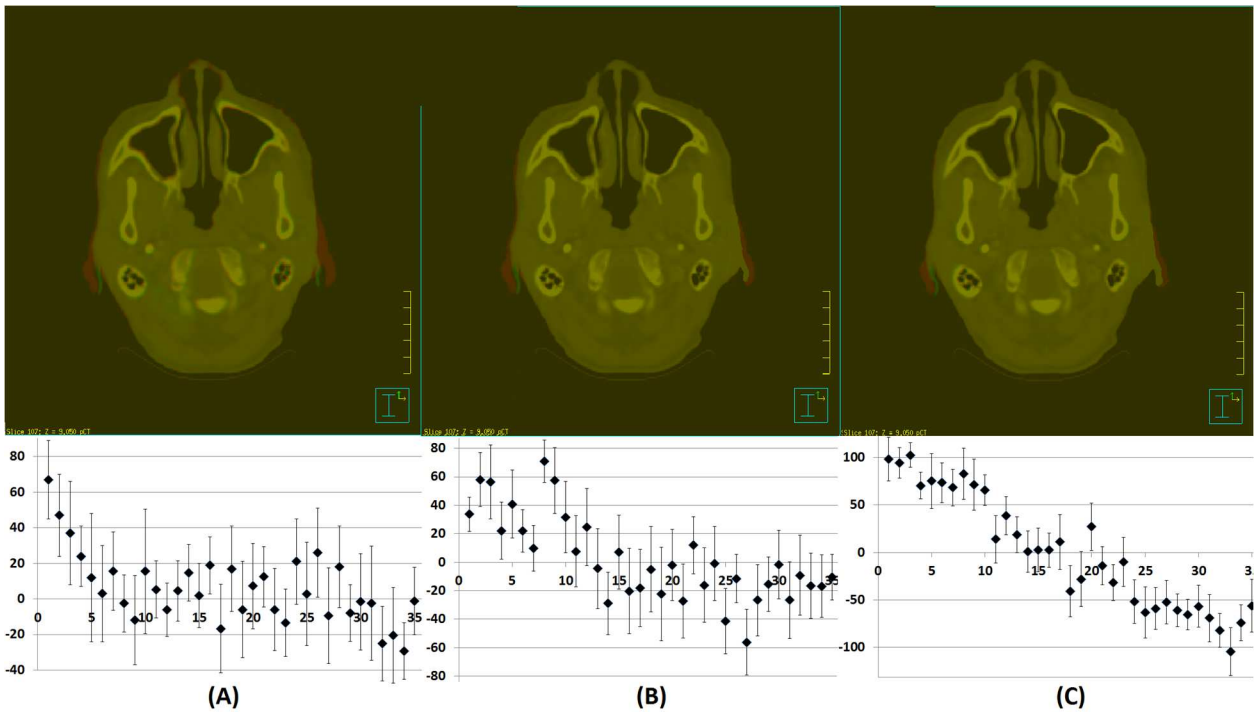

Figure 3.2 RPCA: Results of RPCA models generated from synthetic DVFs for patient A, for whom PCA modeling gave the worst results

Quantitative Evaluation

Figure 3.3 plots mean lengths of the image error vectors, $\|\mathrm{pCT} - \mathrm{epCT}\|$, equations (2.6) and (2.7), as a function of the number of fractions F from which the RPCA model is generated: Patient A, RPCA model generated from clinical CBCTs and DVFs; patient D, RPCA model generated from clinical CBCTs and DVFs; patient A, RPCA model generated from synthetic wCT and DVFs; patient D, RPCA model generated from synthetic wCT and DVFs.

Although plotted against F = 5, 18, 34, clinical RPCA models utilized the first 5 CBCTs, approximately half of available CBCTs, and all but the final CBCT. Vector lengths are scaled by $1/\sqrt{M}$ and plotted points are shifted slightly horizontally to avoid overlap of

the error bars. SPCA model results (similar to the Figure 2.7) also plotted on Figure 3.3 as a grey dashed lines for comparison.

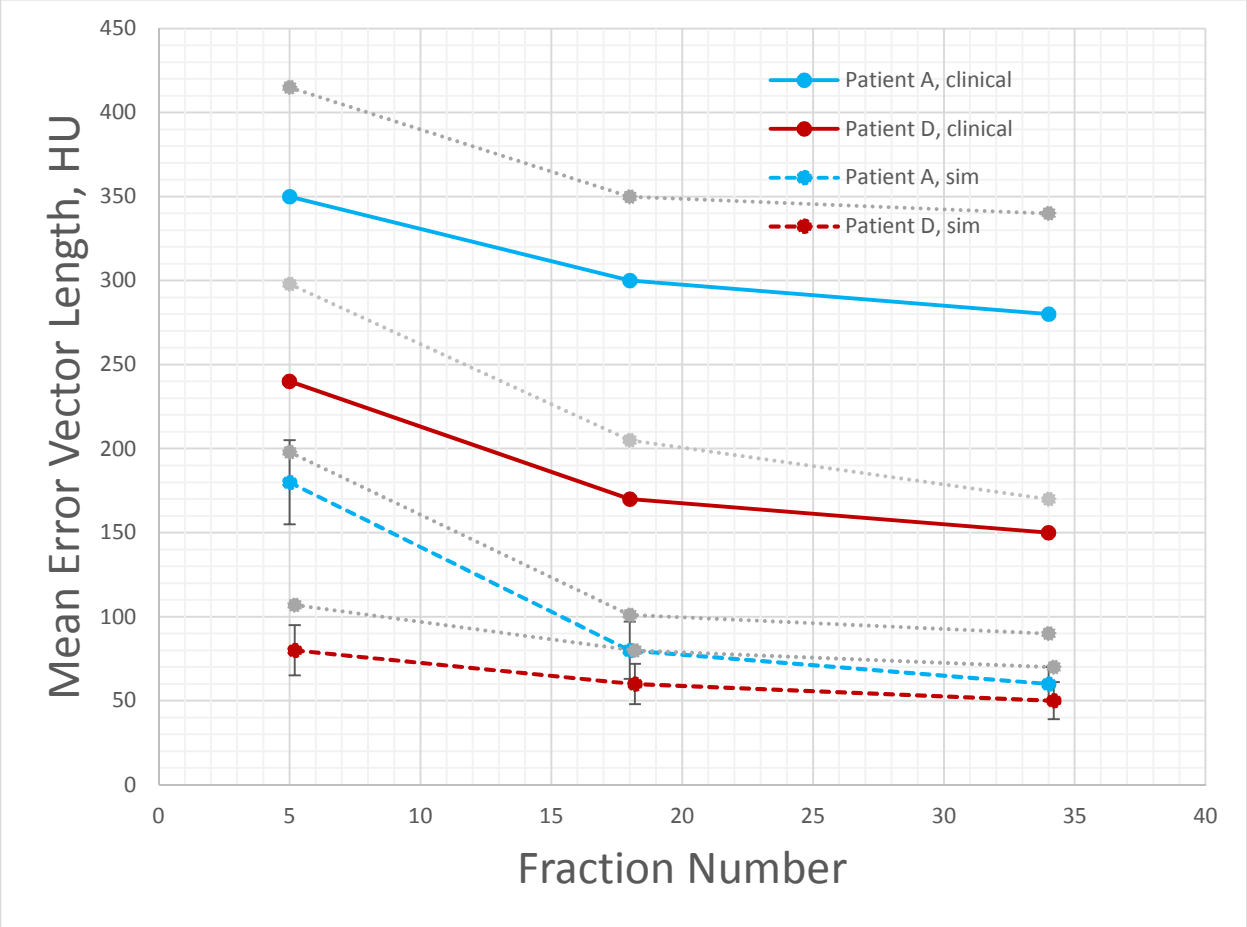

Figure 3.3 RPCA: Mean lengths of the image error as a function of the number of fractions F. Vector lengths are scaled by $1/\sqrt{M}$. Both the mean and standard deviation of the lengths of the image error vectors decrease as F increases. SPCA results are represented by dashed grey lines.

Table 3.2 shows results of gamma analysis of epCT versus pCT. Specifically, it shows the percentage of gamma values exceeding one, using 3%/3mm criteria for the simulated and clinical cases of patients D (best case out of 10 patients) and patient A (worst case out of 10) for the RPCA models generated from first 5 fractions, half of the treatment fractions and all-but-last fraction. Gamma analysis results for the SPCA models are shown in the parentheses.

		Patient D (best case out of 10 patients)	Patient A (worst case out of 10 patients)
Simulated	5 FX	0.15 (*0.25*)	0.42 (*0.50*)
	HALF	0.08 (*0.14*)	0.17 (*0.24*)
	ALL_BUT_LAST	0.06 (*0.11*)	0.10 (*0.18*)
Clinical	5 FX	2.13 (*2.39*)	3.83 (*4.15*)
	HALF	1.13 (*1.33*)	1.91 (*2.07*)
	ALL_BUT_LAST	0.97 (*1.15*)	1.64 (*2.02*)

Table 3.2 RPCA: Results of gamma analysis of epCT versus pCT: percent gamma values exceeding one, using 3%/3mm criteria. Gamma analysis results for the SPCA models are shown in the parentheses.

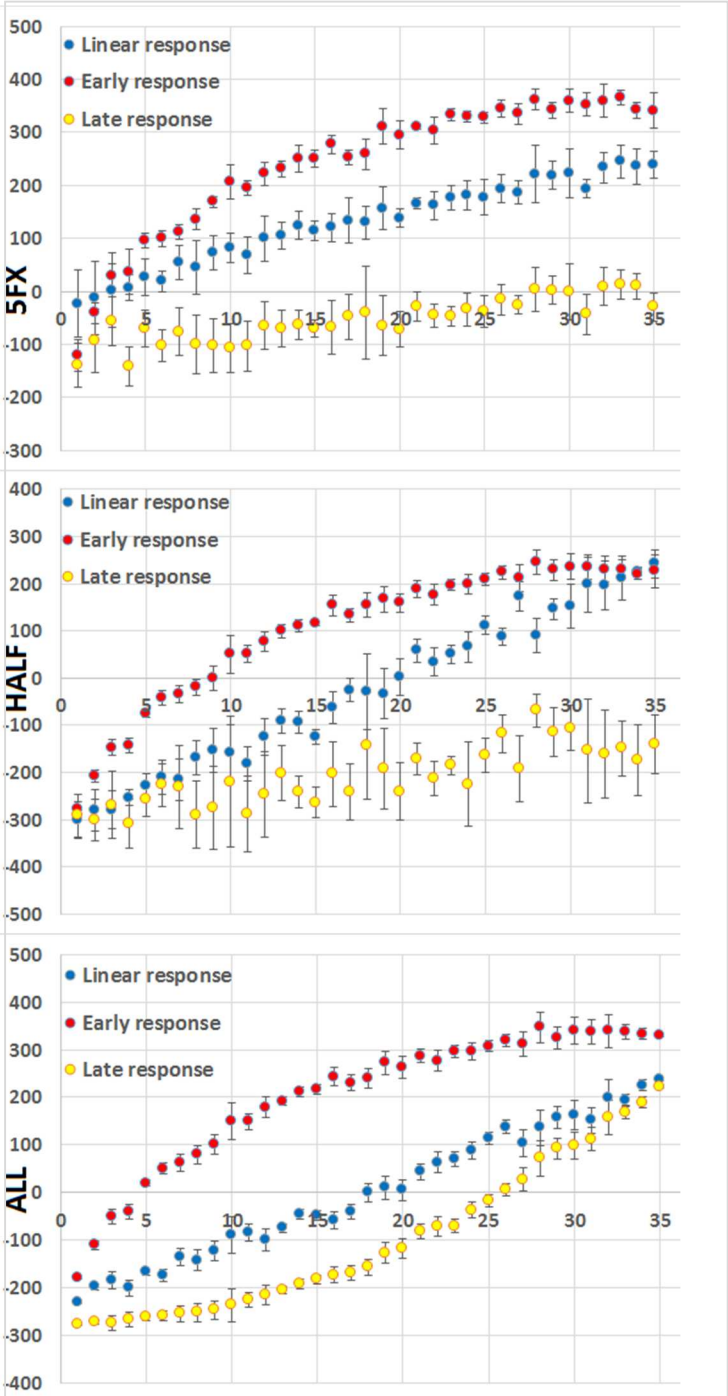

Figure 3.4 Leading EDVF weight averaged for SPCA and RPCA models generated from synthetic DVFs for a patient who experienced parotid shrinkage. Results are shown for the PCA models generated from first 5 fractions (top), half of the fractions (middle) and all-but-last fraction (bottom)

Figure 3.4 shows averaged results for RPCA models generated from synthetic DVFs for a patient with parotid shrinkage. In these models, κ (equation (2.1)) is equal to one. Each panel shows the projection of synthetic DVFs onto the leading EDVF (i.e., weight $\widehat{w}_{f,1}$ from step M1 Chapter 2, Materials and Methods). The top panel shows results for PCA models built from the first 5 of 35 CBCTs; middle panel, 18 CBCTs; bottom panel, 34 CBCTs.

Each panel in Figure 3.4 shows weights for the linear, early and late response models (section 2.4). To generate each curve, RPCA models were created for 5 simulated treatment courses. Plotted data points are mean

weights. The error bars represent ± one standard deviation around the mean.

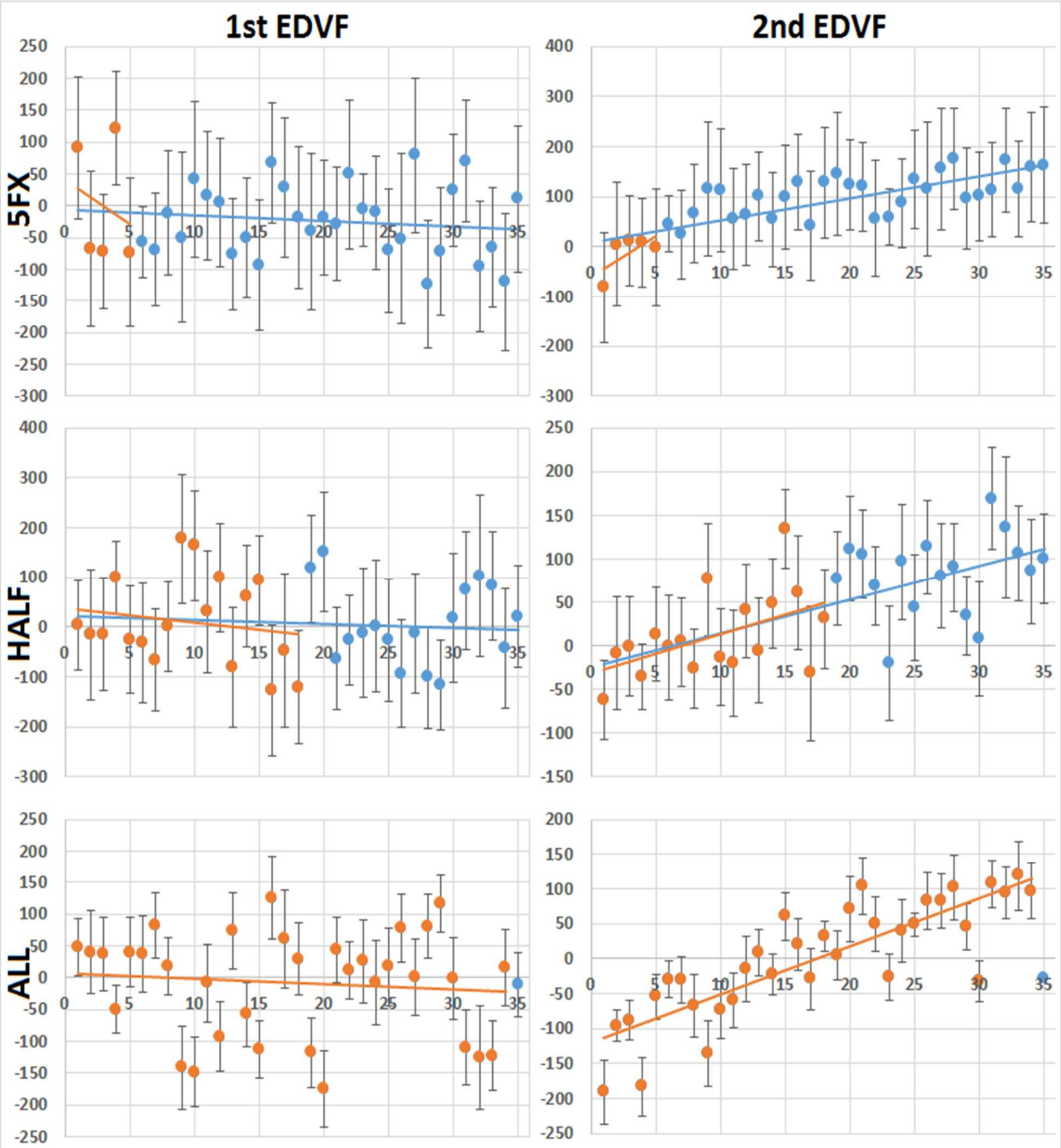

Figure 3.5 RPCA: 1st and 2nd EDVF weights for RPCA models generated from synthetic DVFs for a patient who experienced parotid shrinkage. A linear response model was assumed (Chapter 2, Materials and Methods), and $\kappa = 5$ in equation 2.1, ensuring that DVFs incorporated approximately 5 times the level of random motion seen in clinical CBCTs

Figure 3.5 shows results for RPCA models generated from synthetic DVFs for a patient who experienced parotid shrinkage. Left and right columns show the projections of synthetic DVFs onto the two leading EDVFs. A linear response model was assumed and κ was equal to 5, ensuring that the magnitude of fraction-to-fraction random motion was exaggerated to approximately 5 times the level seen in clinical CBCTs, making it more difficult for PCA to extract systematic change from the random background.

As in Figure 3.4, plotted points on Figure 3.5 are the means of 5 simulated courses, and error bars represent $\pm$ one standard deviation. Orange points show the EDVF weights for the first F fractions, synthetic DVFs for which were included in the RPCA model (first 5, half and all-but-last). Blue points show weights for fractions F+1,..., N, synthetic DVFs for which were excluded from the RPCA model. The orange line is the regression line for orange points. The blue line is the regression line for all points, orange and blue. Orange regression lines match the intercept ρ and slope σ in equation 2.4. No blue linear regression line is shown for the RPCA model generated from all-but-last fraction.

Figure 3.6 shows results for the RPCA models generated from clinical DVFs for a patient who experienced weight loss in the left neck. In this case, plotted points are projections of the clinical DVFs onto the first three EDVFs. Higher EDVFs (4+) were omitted since they accounted for <10% of the total variation. Since clinical data is being used, there is only one treatment course, and no error bars are plotted. Orange and blue points and lines are as in Figure 3.5.

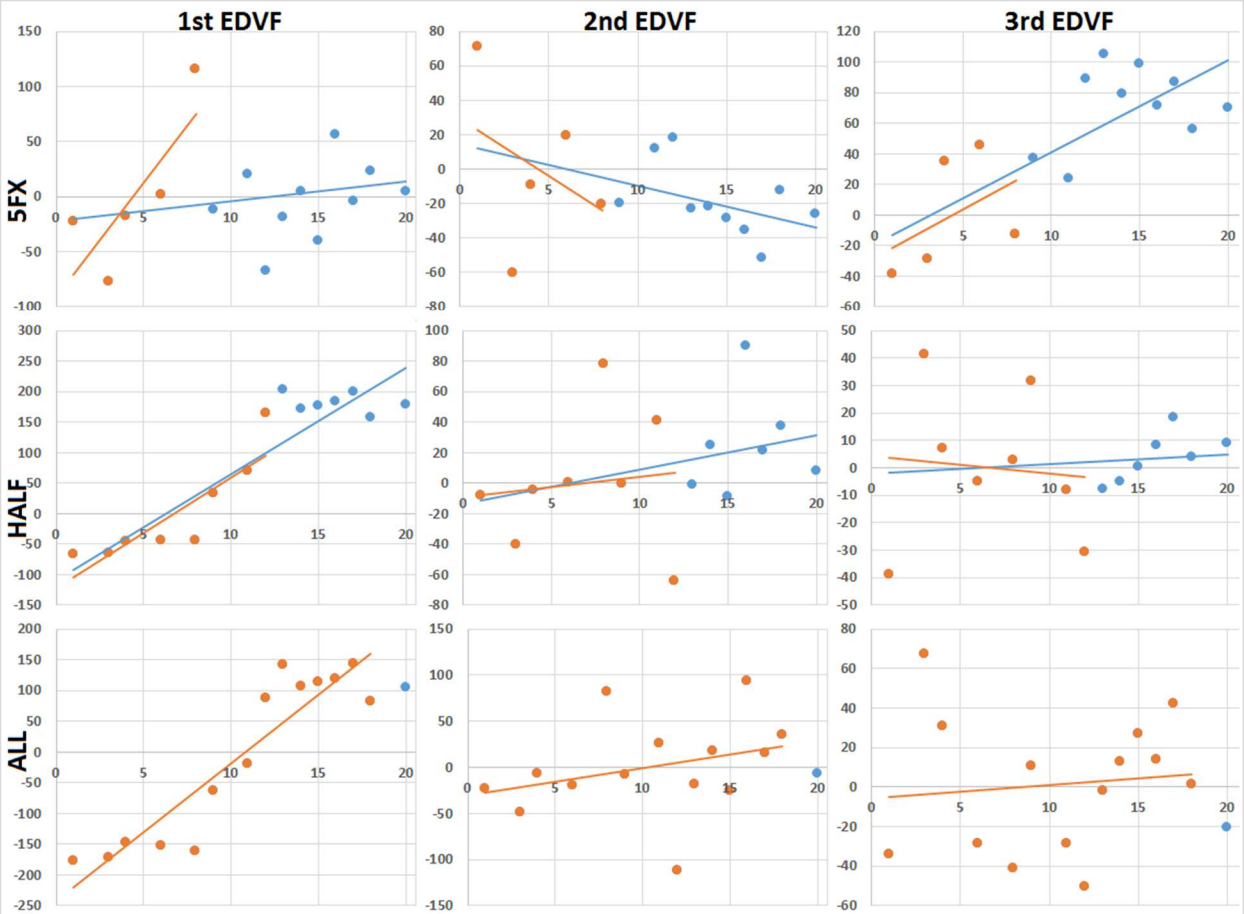

Figure 3.6 RPCA: 1st, 2nd and 3rd EDVF weights for RPCA models generated from clinical DVFs for a patient who experienced weight loss in the left neck

Figure 3.7 shows additional results — predicted DVFs and eigenimages — for the same patient and clinical DVF data as in Figure 3.6. Columns 1 and 2 give results for SPCA models, columns 3 and 4 for RPCA models. DVFs (green arrows, columns 2 and 4) were generated using equation (5) with K = 3 EDVFs, and the same orange regression lines as shown in Figure 3.7.

In Figure 3.7, DVF arrow directions represent pull-back displacement fields from the planning anatomy (pCT) to the final treatment fraction. DVFs are superimposed on

the pCT image set to facilitate visual evaluation. Figure 3.7 shows DVFs for the same axial slice through the patient anatomy.

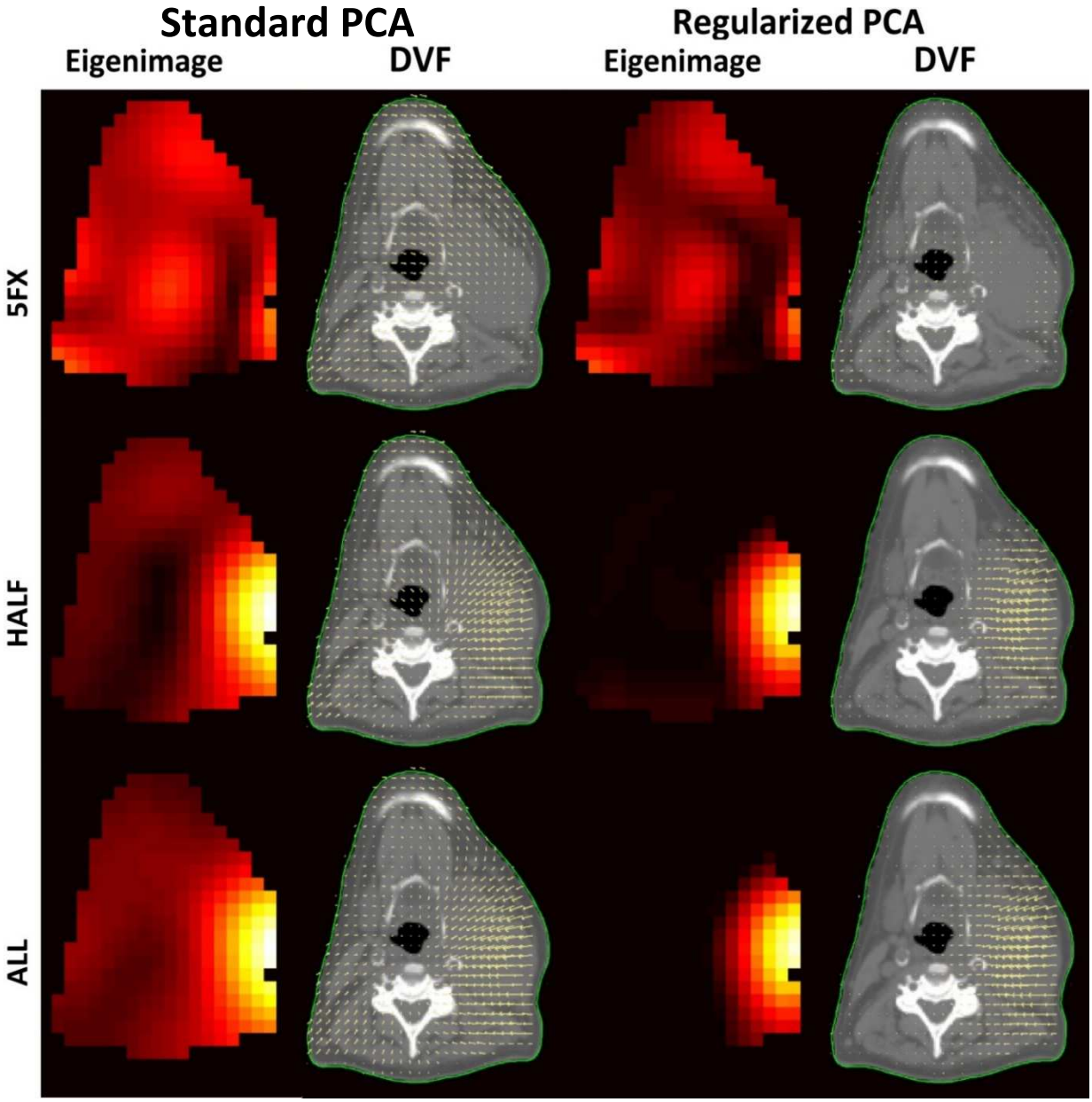

Figure 3.7 RPCA: Predicted DVFs and corresponding eigenimages (heat map representation of DVF vector magnitudes) for the same patient as in Figure 3.7. DVF arrow directions represent pull-back displacement fields from the planning anatomy (pCT) to the final treatment fraction. The magnitude of displacements is at the same scale as the background image.

The eigenimages in columns 1 and 3 of Figure 3.7 are heat-map representations of the DVFs' vector magnitude. Colors range from white (large magnitude displacements) to red (intermediate magnitude displacements) to black (small or zero displacements). The eigenimages are for the same axial slice as the DVFs.

Figure 3.8 shows the results similar to that shown on Figure 3.7, but for the patient with parotid shrinkage and weight loss as a major anatomical change during radiotherapy.

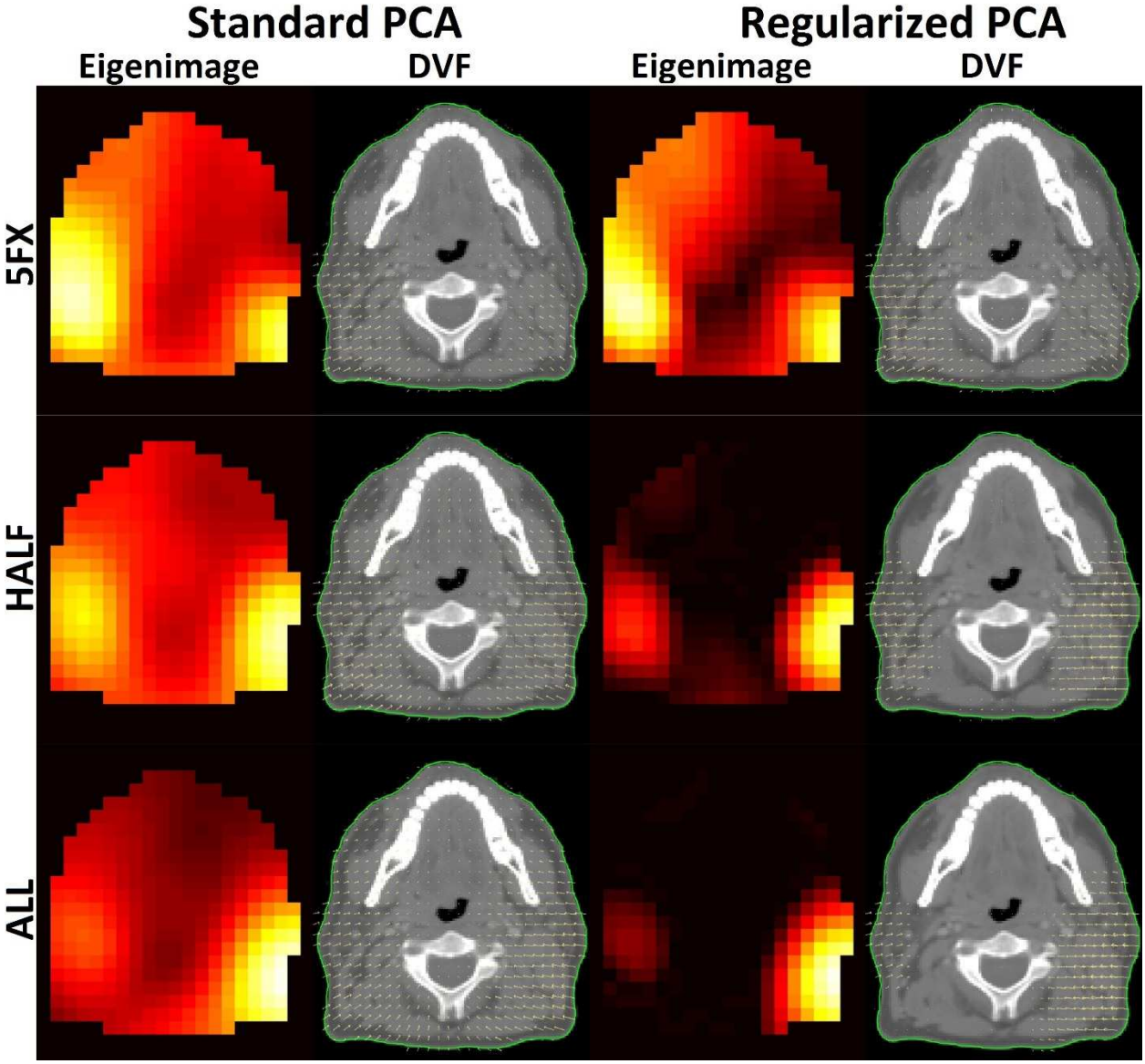

Figure 3.8 RPCA: Predicted DVFs and corresponding eigenimages (heat map representation of DVF vector magnitudes) for the patient with parotid shrinkage and weight loss as a major anatomical change during radiation therapy.

Discussion

Qualitative Evaluation

Table 3.1 shows that R^2 coefficients for the simulated linear cases for the first EDVF have values close to 1, while EDVFs 2-5 produce much lower R^2 values. This result shows that the leading first EDVF can capture the simulated linear major mode of anatomical change, while succeeding EDVFs capture residual errors and noise.

Figure 3.1 shows that RPCA modeling is capable of extracting the major mode of anatomical change during head and neck radiation therapy. The leading EDVF coefficients show a smooth progression during treatment, and the more CBCTs that are included in the PCA model, the better the model becomes. This is indicated by a progressive tightening of the standard deviations of EDVF weights as one moves from model A (5 fractions), to model B (18 fractions), to model C (34 fractions).

In Figure 3.1 the modeled anatomical change, left neck lymph node shrinkage, is large — it affects a relatively large volume of the patient's anatomy. RPCA searches for EDVFs that can explain variability across CBCT images. The modeled anatomical change is large, and, similar to SPCA, the RPCA technique is easily able to 'extract' the major deformation mode(s) from noisy data.

In Figure 3.2 (patient A, worst case for SPCA model), the modeled anatomical change, bilateral parotid shrinkage, is relatively small — it affects a localized volume around the parotids. In this case, as with the case on Figure 3.1, RPCA also successfully isolates systematic anatomical change from other random variations. This is the opposite of the SPCA modeling results, which had more difficulty in isolating the anatomical

change from other random variations that are present in the CBCT images. The RPCA model is successful for patient D. The RPCA models for F=5 fraction show a fairly weak linear progression of the leading EDVF coefficient, and the standard deviation of the coefficients is large, indicating that the RPCA technique is having a difficult time 'locking onto' the major deformation mode. But for the case F=18 and 35 the RPCA model become good enough to predict the anatomy, with a higher level of confidence.

One of the conclusions of this study is that RPCA could successfully extract smaller systematic anatomical changes from daily CBCT images.

Quantitative Evaluation

Figure 3.3 shows that larger HU errors occur for the RPCA models generated from clinical CBCTs (lines (a) and (b)), than those generated from synthetic images and DVFs (lines (c) and (d)). Comparing to SPCA, RPCA is more successful in extracting useful models from synthetic cases and clinical CBCT images.

This conclusion is reinforced by the gamma results in Table 3.2. Those results show that the number of voxels in epCT that disagree with pCT by more than 3% or 3 mm is fairly modest for the RPCA models generated from synthetic DVFs, but much larger in models generated from clinical CBCTs. And in all cases RPCA models have a smaller number of voxels which fail the 3% and 3mm gamma criteria than the SPCA models.

As for the SPCA models, quantitative results shown in Figure 3.3 and Table 3.2 may be used as an indirect way of testing the accuracy of DVFs, or the accuracy of the reconstructed epCT versus the pCT image. Results of the quantitative analysis give an idea of how the number of fractions used to build a model and random changes presented

in simulated and clinical data affect the quality of the last-fraction DVF and overall accuracy of the epCT with respect to the pCT image.

PCA Performance

Figure 3.4 illustrates SPCA and RPCA performance under favorable conditions. Figure 3.4 results are for a synthetic DVF set, where by design only one type of systematic change is present in the patient data, and the magnitude of random changes is comparable to clinical CBCTs. As a consequence, the error bars in Figure 3.4 are relatively small, indicating consistent results across multiple simulated treatment courses. Under these conditions, the bottom panel in Figure 3.4 shows that PCA can successfully extract systematic motion using the leading EDVF. In the bottom panel, the curves for early, linear and late response models mirror the profiles in Figure 2.3 (Chapter 2), as one might hope. Figure 3.4 confirms that under favorable conditions — i.e., given sufficient patient data to enable extraction of mean trends in the presence of random background — PCA modeling can accurately extract the time-profile of anatomical change.

For all response models, SPCA and RPCA perform well when able to build a model from 34 fractions (Figure 3.4 bottom panel). When it is limited to half of the fractions (middle panel), or the first 5 fractions (top panel), PCA continues to perform well for the early and linear response models — the red and blue curves in the top 2 panels mirror those in the bottom panel. However, it fails for the late response model in that the profile of the late response weights in Figure 3.4, top and middle panels, does not mirror the late response model of anatomical changes as shown in Figure 2.3. This illustrates an

intuitively obvious fact. PCA can only be successful if it is given sufficient motion data from which to build a model. In the late response model, there is simply not enough information present in early fractions for PCA to build a valid model.

The ability of SPCA and RPCA to generate patient-specific models from initial treatment fractions for late-responding patients will depend on factors such as the size of anatomical change relative to random motion, and will likely need to be evaluated on a treatment site-by-site basis. A possible alternative is to develop population-based PCA models of anatomical change, and use these as a starting point for all patients. Each patient's motion model could then be refined as patient-specific data is acquired over the course of treatment. This work considers only patient-specific SPCA and RPCA models, generated from a single patient's data. Population based models represent a direction for future research, and are not considered here. However, one might hope that population-based models, based on large volumes of clinical data, could approach the PCA results shown in the bottom panel of Figure 3.4.

Figure 3.5 illustrates (only) RPCA performance under challenging conditions. Figure 3.5 results are for a synthetic DVF set, where by design only one type of systematic change is present in the patient data, but where the magnitude of random changes is exaggerated with respect to clinical CBCTs. As a consequence, the error bars Figure 3.5 are large, indicating a high degree of variability in DVFs across simulated treatment courses. Under these conditions, the bottom two rows of Figure 3.5 show that RPCA is still able to successfully extract systematic change when it has access to 18 of 35, or 34 of 35, fractions. Note that the regression lines in row 2 agree with those in row 3, suggesting that RPCA is consistently identifying the same mode of motion in each EDVF.

What is new in this scenario is that RPCA now captures motion in more than one leading EDVF. Figure 3.5 column 2 shows that the 2nd EDVF weight has non-zero slope, indicating that it plays a role in modeling motion. For realistic motion scenarios, it is expected that PCA will require more than one EDVF in order to faithfully model anatomical motion.

The top row of Figure 3.5 shows that RPCA breaks down when it only has 5 fractions of data. In this scenario, the orange regression lines based on the first 5 fractions do not match the blue regression lines based on 34 fractions. The blue lines agree with lower plots, and so can be assumed to represent the 'true' EDVF weights. Predicted DVFs based on the orange regression lines would be wildly inaccurate for later fractions, and so produce erroneous predictions of anatomical change, cumulative radiation dose, etc. This reinforces the conclusion that patient-specific PCA models may have limited utility when based on a small number of initial fractions. As noted above, it may be desirable to investigate population-based models to address this limitation.

Figure 3.5 shows results only for a linear response model. The size of error bars in Figure 3.5 will make it difficult to reliably predict non-linear trends. One could fit different non-linear curves to patient-specific EDVF coefficients, but the confidence intervals around the fits may be large. If, however, one were to generate population PCA models based on large volumes of H&N patient data, one could reasonably hope that average trends could be extracted. Use of regularized PCA to generate population models remains a subject for future research.

Figure 3.6 illustrates PCA performance for a clinical case, where the motion that is present in the H&N CBCT image set is not known a priori. Figure 3.6 results are

qualitatively similar to those in Figure 3.5. They exhibit similar levels of noise (scatter of plotted points around the trend lines) as seen in Figure 3.5. As in Figure 3.5, the orange and blue trend lines in the lower two rows of Figure 3.6 are in good agreement, suggesting that RPCA is consistently identifying the same mode of motion in each EDVF. The orange trend lines in row 2 are in reasonable agreement with the blue lines in rows 2 and 3, showing that an RPCA model based on 18 of 35 fractions can accurately predict EDVF weight trends for remaining fractions. Note that the trend line associated with each EDVF can reasonably be interpreted as systematic anatomical change, while the scatter of points around the trend line represents the superimposed effect of random fraction-to-fraction motion. The consistent trend lines in rows 2 and 3 show that RPCA is consistently identifying the systematic component of anatomical change.

The top row of Figure 3.6 shows that PCA performs poorly when the model is based on only the first 5 fractions. The orange trend lines do not agree with the blue trend lines for EDVFs 1 and 2. This conclusion is consistent with the results for simulated DVFs in Figures 3.4 and 3.5: patient-specific PCA models may have limited utility when based on a small number of initial fractions.

In practice, weights on Figure 3.6, acquired from the projection of the clinical DVFs onto the calculated EDVFs, are used to build a patient-specific RPCA model using equation 2.4. For the RPCA models generated from the first F fractions (e.g., first 5 fractions, half of the fractions, or all-but-last fraction), subsequent weights of the F+1,…, N fractions are calculated using a linear fit, and these weights are then used in equation 2.4 to model future fractions DVFs and corresponding anatomy.

Figures 3.7 and 3.8 provide a visual comparison of the SPCA and RPCA models which were used to calculate the last fraction DVFs from the first 5, half, and all-but-last fraction, and visual confirmation that RPCA is better than SPCA at identifying the systematic component of H&N anatomical change. For reasons discussed below, SPCA tends to produce noisy EDVFs, which are difficult to relate to clinically observable changes. In Figures 3.7 and 3.8, SPCA EDVFs are non-zero across the whole patient anatomy, even though dominant change is clearly confined to the left neck. In contrast, at least when RPCA models are based on 18+ fractions, RPCA is successful at isolating the dominant mode of change to the left neck area. RPCA's ability to identify and reproduce clinically observed change creates the potential to use RPCA to anticipate and trigger adaptive re-planning decisions, and for quantitative treatment response assessment.

Prior Applications of PCA

The idea of using PCA in radiotherapy is not novel. For example, the PCA techniques were used to model patient-specific inter-fractional organ deformations in prostate/rectum/bladder[45]. The results of that work showed that geometric variability is governed by only the first few patient-specific eigenmodes, and using first 4 eigenmodes to model organ deformations reduces residual errors to ≤2 mm. The results were later used to assess the dosimetric detrimental effects that inter-fractional organ deformations can have on a planned dose distribution[47]. Coverage-based treatment planning techniques for prostate cases were also proposed based on the PCA organ deformation model[62]. Furthermore, a population-based PCA model was developed and applied to

prostate cases[40], showing that using the first 7 eigenmodes for patients in a database, and first 15 eigenmodes for patients not in a database, reduces residual errors to ≤1 mm.

The main difference between this research and those described above is that this work is focused on separating systematic changes in patients' anatomy from random changes. While this may not be necessary for the prostate/bladder/rectum cases, since these areas don't experience major systematic change during the radiotherapy, this separation is important for H&N cases, since the anatomy could change significantly during the treatment course.

The PCA model in H&N patients was also described and performed to create an organ sample generator (OSG) for expected treatment dose construction[63]. The OSG generated random samples of organs of interest during the treatment course to evaluate dosimetric effects of the organ variations/deformations. The accuracy of the OSG improved with the number of treatment fractions used for the PCA model, showing discrepancy of the dose estimation within 1% for most organs after the first 3 weeks of treatment. The OSG is a useful tool for dose accumulation estimation during the treatment, but since it's not trying to separate systematic changes in anatomy from random changes, it could not be used in the prediction of the end-of-treatment anatomy.

Potential for Regularized PCA

ART promises to improve the quality of treatment received by radiation therapy patients. However, adoption of ART has been held back by some practical considerations. Repeatedly re-planning patient treatments can be costly, in terms of physician and dosimetrist time and physics resources to check and QA treatment plans. There is

consequently a need for measurement-based models of anatomical change and treatment response that would allow physicians to make educated decisions about when to re-plan, which patients will benefit, etc.

RPCA has the potential to solve some of these challenges. RPCA is designed to extract major modes of deformation from noisy imaging data, in principle allowing one to discriminate real changes in the anatomy from background noise. If successful, RPCA could be used to predict the future anatomy, and make re-planning decisions based on dosimetric impact to the tumor and normal tissues.

SPCA is a well-known tool to find the major modes of variations in real-world datasets. However, it was developed for datasets where the dimension of the problem is less than the number of available data samples. In the present problem, the dimension of the problem is 3M (i.e., 3 times the number of DVF voxels), which is on the order of 10^4-10^5 for H&N voxel grids, and therefore much larger than the number of available CBCTs. In this scenario SPCA models are extremely under-determined. As a result, SPCA has a tendency to produce EDVFs than are noisy, and difficult to relate to clinically observable anatomical changes.

RPCA addresses the problem of under-determination by supplementing SPCA with additional constraints on eigenvectors. In the present work, RPCA adds smoothness and sparseness constraints to SPCA. This has the effect of forcing EDVFs to be smooth (i.e., physically realistic) and sparse (i.e., confined to localized regions of anatomy where change is detected). Together, these constraints have a tendency to concentrate detected anatomical change into a smaller number of leading EDVFs, which in turn makes it easier

to relate the EDVFs to clinically observable response. The application of regularized PCA to adaptive radiation therapy is a novel contribution of this work.

This work can be considered to fall within radiomics, which studies how to extract quantitative information from the medical images in order to characterize treatment response. In the present case, RPCA is being used to reduce high-dimensional imaging data to a small number of anatomical motion modes. Detecting tumor deformation during treatment will permit assessment of treatment response. Similarly, detecting the response of normal tissues, such as parotid glands, may permit quantitative evaluation of radiotherapy-related complications.

Study Limitations

Acquiring accurate DVFs between patient images is a key step in this study because the results of PCA modeling are dependent on the quality of input DVFs. Therefore, the choice of DIR algorithm and its registration parameters is one of the most important factors for accurate modeling. In this study Pinnacle's diffeomorphic demons algorithm[58] was used for deformable registrations. Although we visually verified the registration results, use of a different algorithm may produce slightly different results from those presented in this study. In this work other DIR algorithms were not used apart from those implemented in Pinnacle®, since all the codes for DVFs manipulations were implemented considering Pinnacle's® DVF internal structure and performed using Pinnacle® plugin functionality. One of our intended future works is to use different commercial and open-source DIR algorithms to understand the effects on the resultant PCA models.

Quantification of DIR/DVF accuracy is a major challenge for adaptive radiation therapy, on which much research is being expended. It is outside the scope of this work to attempt to quantify the accuracy of DIR algorithms. Instead, we expect that reliable DIR algorithms will emerge from ongoing research and clinical use. Although DVF accuracy will have an impact on the accuracy of PCA models, we note that regularized PCA may be part of the answer to this issue. RPCA has the potential to extract smooth and physically meaningful EDVFs from noisy CBCT data, including the noise introduced by DVF uncertainties. One can reasonably hope that RPCA models will be insensitive to small scale uncertainties present in DVFs, and instead extract larger scale anatomical changes corresponding to observable clinical change.

One other important study limitation is the CF used to acquire DVFs. In this study, CF of 7 was used, which reduces the precision of acquired DVFs compared to non-compressed DVFs. This, in turn, reduces the precision of the motion model and could underestimate the effects of anatomical motion presented in the patient. This effect can be seen in Figures 3.1 and 3.2 – on the left neck lymph node shrinkage (Figure 3.1) and parotid shrinkage (Figure 3.2). RPCA does not precisely capture these anatomical changes due to the large CF used, and epCT is not completely matched to the pCT image, even though it still shows better performance than SPCA, giving an advantage of better smoothness and sparseness due to the regularized approach.

The regularized approach in PCA requires a calculation of penalty matrix of very large size, ~ $(3M)^2$, which puts very high requirements on computational resources. In this work, CF of 7 was used, and random-access memory (RAM) of ~ 100-120 GB (depending on the patient) was required, and calculation time was ~ 7 days on the Wayne

State University High Performance Computing Grid. The calculation time potentially could be improved by using a parallel computing – dividing the calculation of the penalty matrix for RPCA models between multiple processes.

Conclusion

For H&N patients treated with external beam radiation therapy, a PCA model (both standard and regularized) is a potential tool to identify patient anatomy changes early in the treatment course, and use these to make educated adaptive re-planning decisions. This study used synthetic (but realistic) DVFs, as well as clinical CBCTs, to evaluate the ability of the PCA method to extract useful models of anatomical change. In particular, a primary goal of this work was to evaluate the ability of PCA to separate systematic from random changes present in CBCT images.

The study shows that both SPCA and RPCA can capture the major mode of systematic anatomical deformation in the leading EDVF. However, the SPCA approach is most successful at identifying large changes (e.g., significant lymph node shrinkage), and less successful at identifying small changes (e.g., smaller changes in parotid glands). SPCA is challenged by the variety of deformations and noise in clinical CBCT images, and therefore fails to extract major modes of systematic change that are known to be present. Conversely, the RPCA approach is able to identify smaller systematic changes in the presence of the random fraction-to-fraction changes. The current drawback of the RPCA approach is the time of the calculation and memory requirements.

CHAPTER 4 "DOSIMETRIC ASSESSMENT OF EFFECTS OF SYSTEMATIC AND RANDOM FRACTION-TO-FRACTION ANATOMICAL CHANGES IN HEAD AND NECK PATIENTS"

Introduction

Decisions about whether to perform ART for a specific H&N patient could be made by the physician by either comparing the patient's daily anatomical images (like CBCT) with the pCT image and deciding if anatomical changes are large enough to significantly alter the planned dose distribution, or by evaluating the mask used for patient immobilization and positioning, or using other subjective indicators, such as the physician's experience in such cases. Currently, there are no clear quantitative indicators regarding whether or not perform ART for a specific patient[64].

Using advanced treatment techniques like IGRT, one of the potential quantitative indicators for ART in H&N patients could be the measuring of the actual dose delivered to date to targets and OARs, which could be done by calculating "dose of the day" onto re-sampled CT images using DIR and then accumulating it back onto the pCT[65]. Such "dose of the day" calculations, which would give accumulated dose up to but not beyond the current fraction, can be used in the clinic for tracking the dose delivered to the patient in each fraction and comparing it with the planned dose distributions. The drawback of this method is that it is retrospective: one can react to OAR overdoses or target underdoses once they have happened, but there is no good basis for anticipating them and correcting them in advance, while one still has maximum flexibility to re-plan and correct the dose distribution.

In this work one of the potential solutions to this problem is presented. Using developed motion models based on RPCA approach (Chapter 3), not only "dose of the

day" is calculated and accumulated, but also dose of the future fractions is calculated on re-sampled "future CT" images. The predicted cumulative dose is then compared to the planned dose, enabling re-planning decisions to be made earlier in the treatment course. Additionally, at the end of the course, the predicted cumulative dose can be compared with the true cumulative dose, to evaluate the accuracy of the RPCA-based dose predictions.

There are two main hypotheses in this study:

H1: RPCA models can quantify deviations between planned and delivered cumulative dose caused by systematic anatomical changes.

H2: RPCA models can quantify deviations between planned and delivered cumulative dose caused by both systematic and random anatomical changes.

This study provides a testing framework to evaluate the accuracy of RPCA-based anatomical models at predicting cumulative dose. Within this framework it is instructive to separately calculate the dosimetric effects of systematic versus random changes. In this way one can assess the relative contributions of systematic versus random changes. One can then make reliable re-planning decisions based on detected systematic changes, and determine PTV margins to absorb residual random changes.

Materials and Methods

Two H&N patients from the dataset described in Chapter 2, who experienced large systematic changes during the course of radiation therapy, were chosen in order to conduct a dosimetric study. The first of the selected patients experienced parotid shrinkage, and was treated with 70Gy in 33 fractions. The second selected patient

experienced parotid shrinkage and weight loss during the course of radiation therapy, and was also treated with 70Gy in 33 fractions. The following work was performed using synthetic DVFs containing known localized anatomical changes, derived from the warped CT (wCT), as described in the "Synthetic Deformation Vector Fields" section of Chapter 2. The corresponding eigenimages and last-fraction DVFs for the second patient are shown in Figure 3.8.

For the purpose of getting the pCT image, the patients were set up head-first supine on a CIVCO H&N board (CIVCO Medical Solutions, Coralville, IA) using a 9-point thermoplastic mask with individually modeled pillow for immobilization. The treatment plan was prepared and optimized within the Eclipse TPS (Varian Medical Systems, Palo Alto, CA) using the Analytical Anisotropic Algorithm (AAA). For daily CBCT images, the following parameters were used: 120 kVp, 20 mA, 150 cm source-to-detector distance.

For the hypothesis *H1*, the cumulative dose was calculated for the systematic change only using the RPCA models described in Chapter 3:

(i) Synthetic DVFs, based on the linear response model, and containing the systematic component only (random excluded) were taken (equation 2.1, with D_R=0) for each of 33 fractions. These DVFs were inverted using the ITK[66] software library: the synthetic DVFs map coordinates from a space of pCT into a space of daily anatomy (i.e. CBCT), and the inverse synthetic DVFs map coordinates from the space of daily anatomy into the space of pCT. These inverse DVFs are then used to get day-of–treatment anatomy from the pCT for each of 33 fractions, which in turn are used to get cumulative dose (dose A). This data simulates anatomies, bi-directional DVFs, and daily CTs for a full treatment course.

(ii) Using the RPCA model (Chapter 3, Materials and Methods) and synthetic DVFs from step (i), predicted DVFs were calculated using first 5, half and all but last treatment fractions. Inverse DVFs and predicted CT images for each of 33 fractions were acquired and used to predict cumulative dose (dose B) at the final fraction.

(iii) The above procedure generates three dose distributions:

- Planned dose: This is the original planned dose distribution generated on the planning CT

- Dose A: For a simulated treatment course, this is the “true” cumulative dose at the end of the course, assuming zero random changes.

- Dose B: For a simulated treatment course, this is the dose predicted by an RPCA model, where the model could be derived from the first 5, half, or all but last simulated fractions, assuming zero random changes.

For relevant structures, Dose Volume Histograms (DVHs) for 3 scenarios were compared: planned dose, dose A, and dose B. If *H1* is correct, the expectation is to see dose A similar to dose B. In this study “similarity” was checked by comparing the maximum and the mean dose deviations between doses A and B which were expected to be close enough to be clinically equivalent. We also expect that doses A and B can differ significantly from the planned dose, depending on structure, due to the presence of significant anatomical changes over the treatment course.

For hypothesis *H2*, the cumulative dose was calculated for both systematic and random changes using the RPCA models:

(iv) Synthetic DVFs, based on the linear response model, and containing both systematic component and 10 different simulations of random components were taken

(equation 2.1) for each of 33 fractions. Using the same procedure as in step (i), these DVFs were inverted and then used to get cumulative dose in the presence of systematic and random components (dose C).

(v) Using RPCA model and synthetic DVFs with simulated random components from step (iv), predicted DVFs were calculated using first 5, half and all but last treatment fractions, inverse DVFs and predicted CT images for each of 33 fractions were acquired and used to get cumulative dose (dose D).

(vi) The above procedure generates three dose distributions:

- Planned dose: This is the original planned dose distribution generated on the planning CT
- Dose C: For a simulated treatment course, this is the “true” cumulative dose at the end of the course, assuming non-zero random changes.
- Dose D: For a simulated treatment course, this is the dose predicted by an RPCA model, where the model could be derived from the first 5, half, or all but last simulated fractions, assuming non-zero random changes.

In the same manner as above, for relevant structures, DVHs for 3 scenarios were compared: planned dose, dose C, and dose D. If *H2* is correct, the expectation is to see dose C similar to dose D, and both of these different from the planned dose.

A CF of 7 was used for this study for the reasons discussed in Chapter 3 – generation of RPCA models using our current method is numerically and memory intensive, so it was necessary to adopt a CF of 7 in order to keep computing resources and execution times within acceptable limits.

However, aggregation of DVF voxels has the effect of smoothing DVFs, reducing

their spatial resolution, at least in the XY-plane. As shown in Chapters 2 and 3 (Figures 2.5, 2.6, 3.1, 3.2), using large CF for the acquisition of the DVFs could underestimate the anatomical motion in the patient even if it was captured correctly in the CBCTs.

To assess this effect, the predicted dose from RPCA models (where anatomical motion could be underestimated due to DVF compression) was compared to the "real" accumulated dose and to the planned dose. "Real" dose accumulation (dose R) was performed in VelocityAI (version 3.2.0, Varian Medical Systems) using the method described in Kumarasiri et al[67]. Acquiring dose R does not require DVFs compression, and therefore it accounts for all anatomical motion, subject to the DIR precision and uncertainty.

Dose R is then compared to planned dose, and doses A, B, C and D. If compressed DVFs in fact underestimate the anatomical changes in the patient, dose R is expected to be different from the planned dose, and the DVHs associated with doses A, B, C and D are expected to be in between the DVH of the planned dose and DVH of the dose R.

The percent differences between the planned dose and simulated (dose A, C), modeled (dose B, D), or accumulated dose (dose R) was calculated using the following equation:

$$\Delta D = \left(\frac{D_{sim/model/accum} - D_{planned}}{D_{planned}}\right) \times 100 \quad (4.1)$$

Results

Figures 4.1 and 4.2 show the DVHs for the left parotids of patients 1 and 2. On these figures, planned DVH (blue) is compared to the calculated DVHs of patients 1 and 2 with the systematic only (Figure 4.1, dose A, green) and systematic and random

components (Figure 4.2, dose C, green) superimposed on this patient during the course of radiation therapy. The anatomy of these patients was also predicted using the RPCA models for the first 5, half and all but last treatment fractions and corresponding predicted DVHs are shown on Figures 4.1 (dose B) and 4.2 (dose D) as purple, dark blue and brown dashed lines respectively.

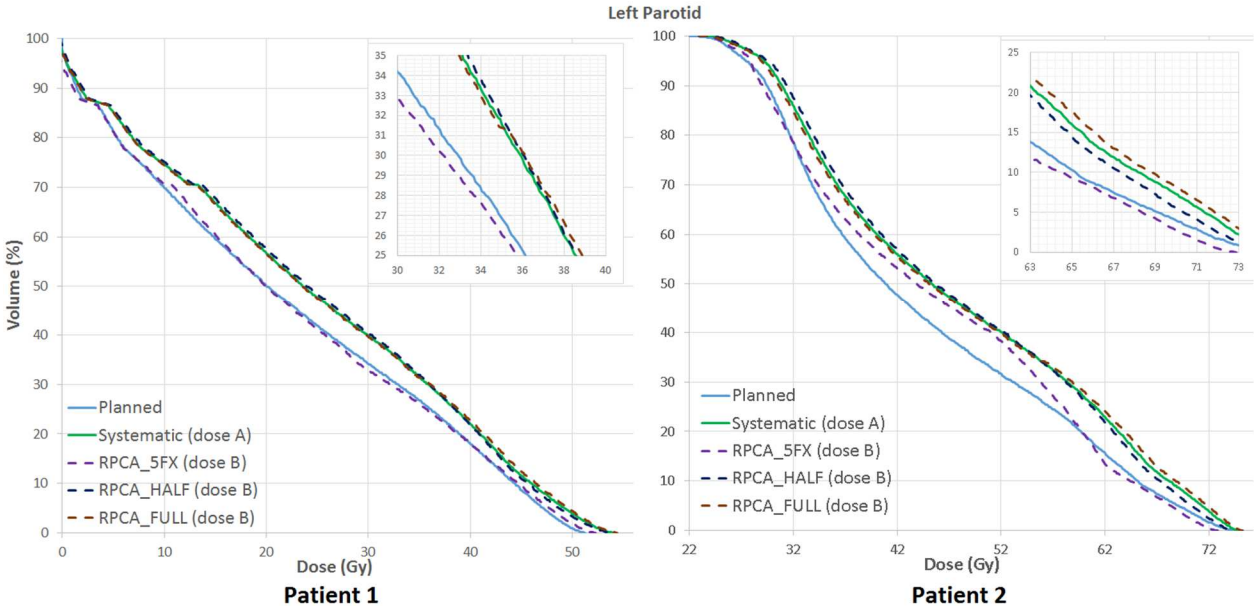

Figure 4.1 DVHs for the left parotids of the patients 1 and 2. Planned DVH (blue) is compared to the simulated DVH (dose A) of the patient with the systematic only component superimposed on the patient's anatomy during the course of radiation therapy, and also compared to the modeled DVHs (doses B) for the predicted anatomies from the RPCA models built using the first 5 (purple), half (dark blue) and all but last treatment fractions (brown).

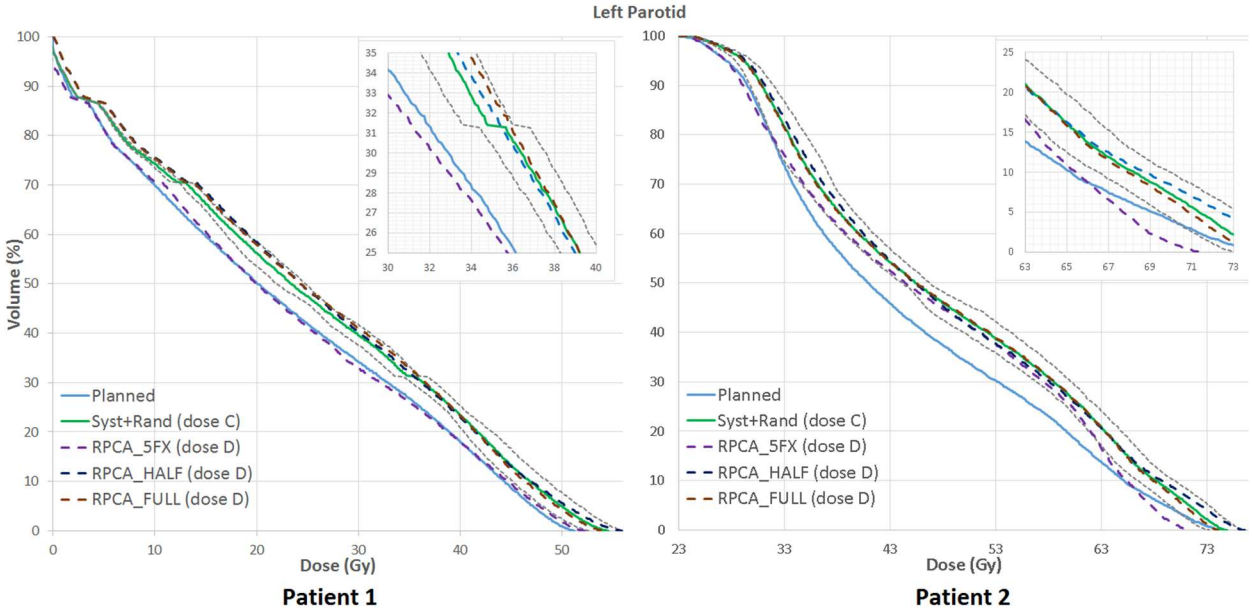

Figure 4.2 DVHs for the left parotids of the patients 1 and 2. Planned DVH (blue) is compared to the simulated DVHs (dose C) of the patient with the systematic and random components superimposed on the patient's anatomy during the course of radiation therapy, and also compared to the modeled DVHs (doses D) for the predicted anatomies from the RPCA models built using the first 5 (purple), half (dark blue) and all but last treatment fractions (brown). Grey dotted lines represent the standard deviation of the green line.

Figure 4.3 and 4.4 show the DVHs for the right parotids of the patients 1 and 2.

The information is similar to that shown in Figures 4.1 and 4.2.

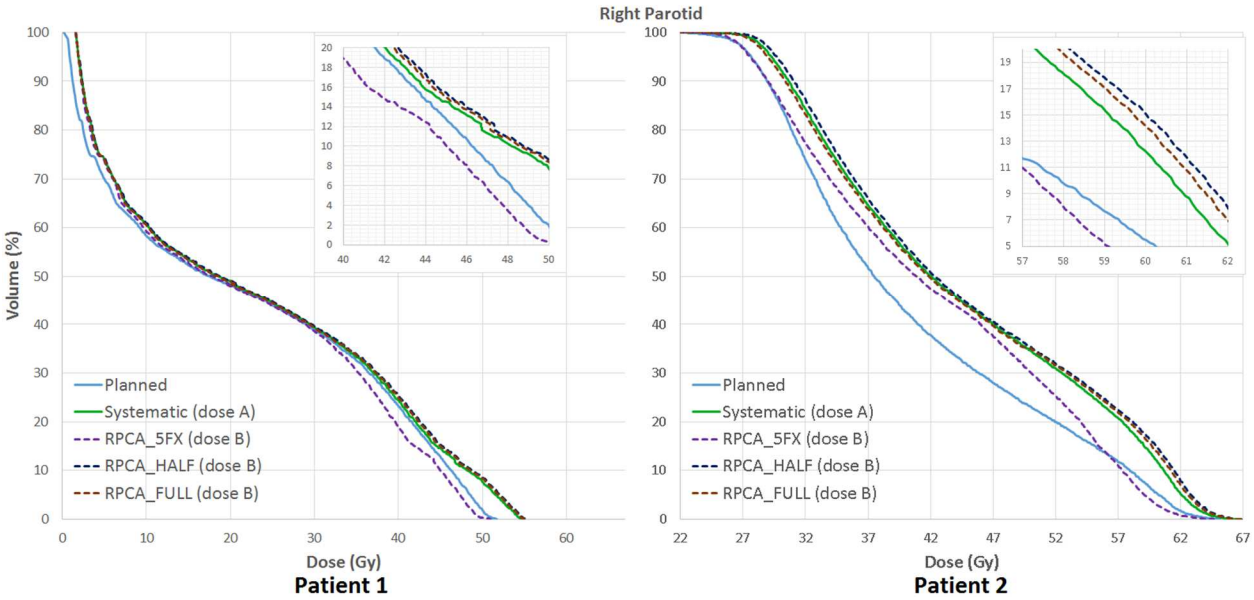

Figure 4.3 DVHs for the right parotids of the patients 1 and 2. Planned DVH (blue) is compared to the simulated DVH (dose A) of the patient with the systematic only component superimposed on the patient's anatomy during the course of radiation therapy, and also compared to the modeled DVHs (doses B) for the predicted anatomies from the RPCA models built using the first 5 (purple), half (dark blue) and all but last treatment fractions (brown).

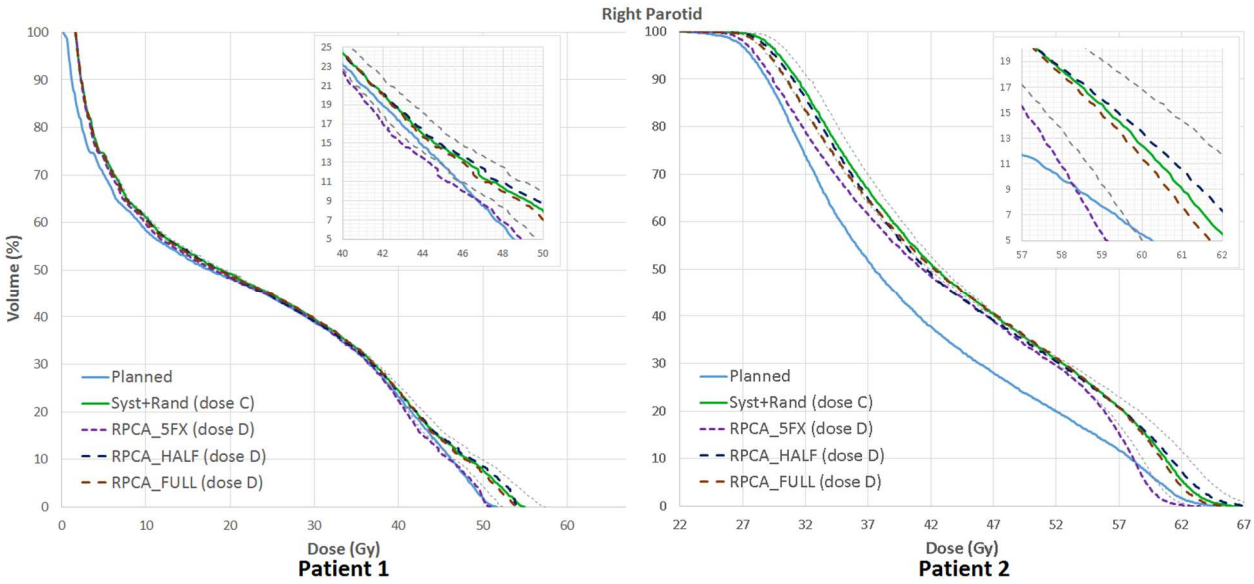

Figure 4.4 DVHs for the right parotids of the patients 1 and 2. Planned DVH (blue) is compared to the simulated DVHs (dose C) of the patient with the systematic and random components superimposed on the patient's anatomy during the course of radiation therapy, and also compared to the modeled DVHs (doses D) for the predicted anatomies from the RPCA models built using the first 5 (purple), half (dark blue) and all but last treatment fractions (brown). Grey dotted lines represent the standard deviation of the green line.

Figures 4.5 and 4.6 show the DVHs for the spinal cords of the patients 1 and 2. The information is similar to that shown in Figures 4.1, 4.2, 4.3 and 4.4.

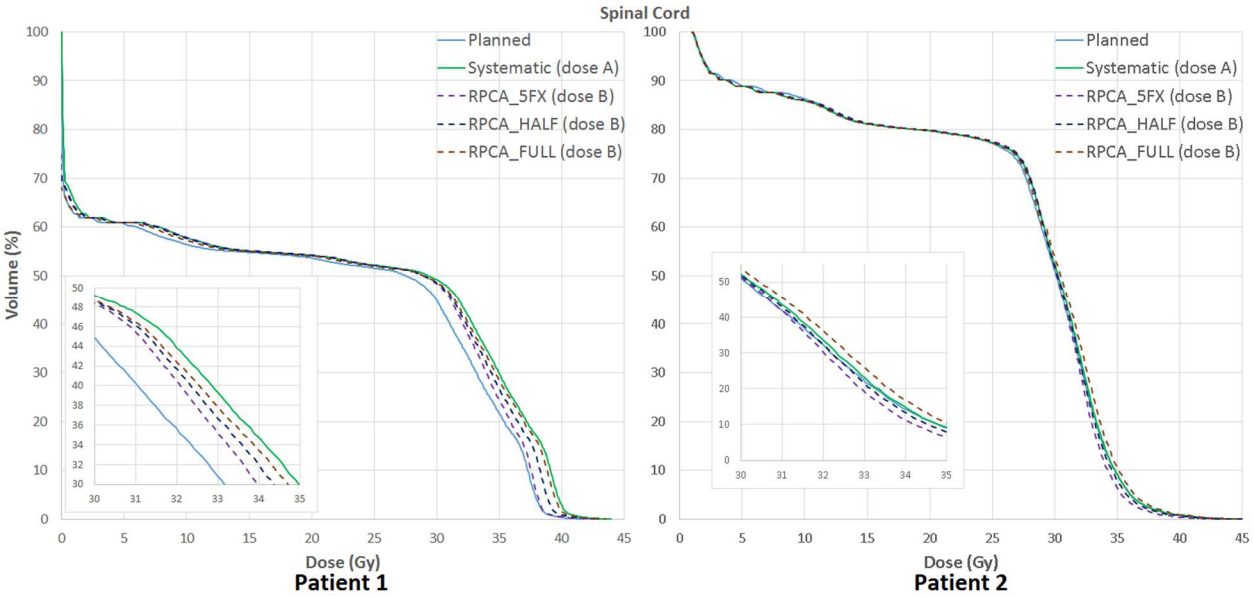

Figure 4.5 DVHs for the spinal cords of the patients 1 and 2. Planned DVH (blue) is compared to the simulated DVH (dose A) of the patient with the systematic only component superimposed on the patient's anatomy during the course of radiation therapy, and also compared to the modeled DVHs (doses B) for the predicted anatomies from the RPCA models built using the first 5 (purple), half (dark blue) and all but last treatment fractions (brown).

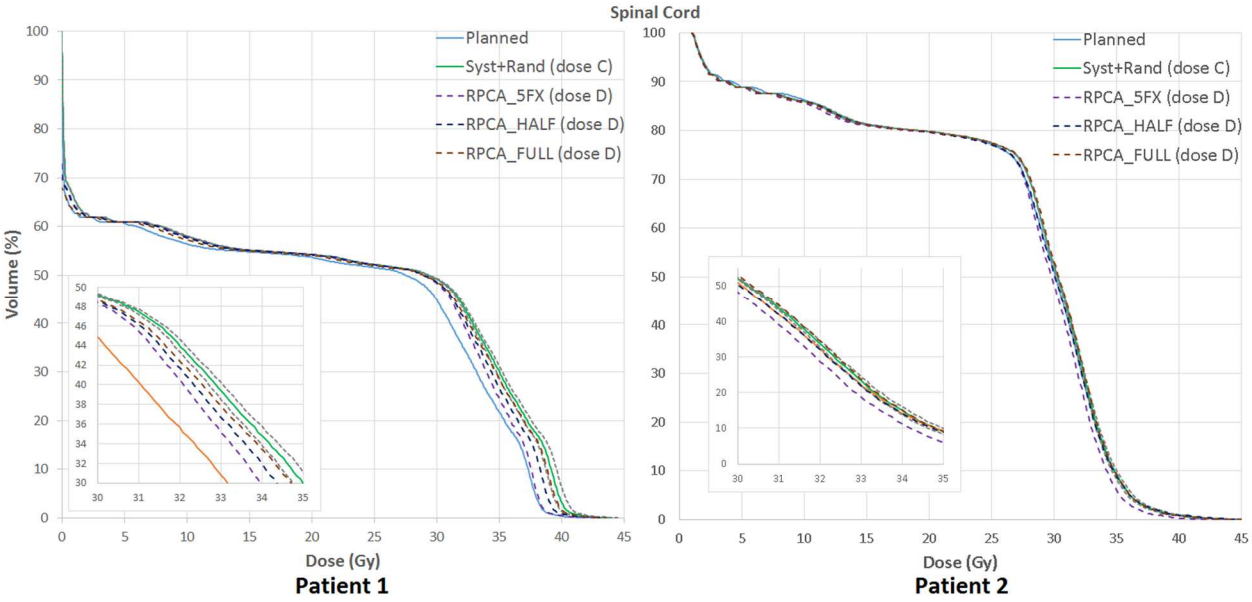

Figure 4.6 DVHs for the spinal cords of the patients 1 and 2. Planned DVH (blue) is compared to the simulated DVHs (dose C) of the patient with the systematic and random components superimposed on the patient's anatomy during the course of radiation therapy, and also compared to the modeled DVHs (doses D) for the predicted anatomies from the RPCA models built using the first 5 (purple), half (dark blue) and all but last treatment fractions (brown). Grey dotted lines represent the standard deviation of the green line.

Figure 4.7 (A) shows the pCT image (red) overlaid on the resampled CBCT image of the last treatment fraction for the patient 2 who experienced parotid shrinkage and weight loss during the course of radiation therapy. The CBCT is resampled using the diffeomorphic demons DVF compressed with a CF of 7. Figure 4.7 (B) shows the pCT image (red) overlaid on the epCT (green) for this patient; the epCT image is acquired using equation 2.4 from Chapter 2. Red arrows show the underestimation of the parotids movement due to the large CF used for the DVFs. Figure 4.7 (C) shows the pCT image (red) overlaid on the last fraction CBCT image.

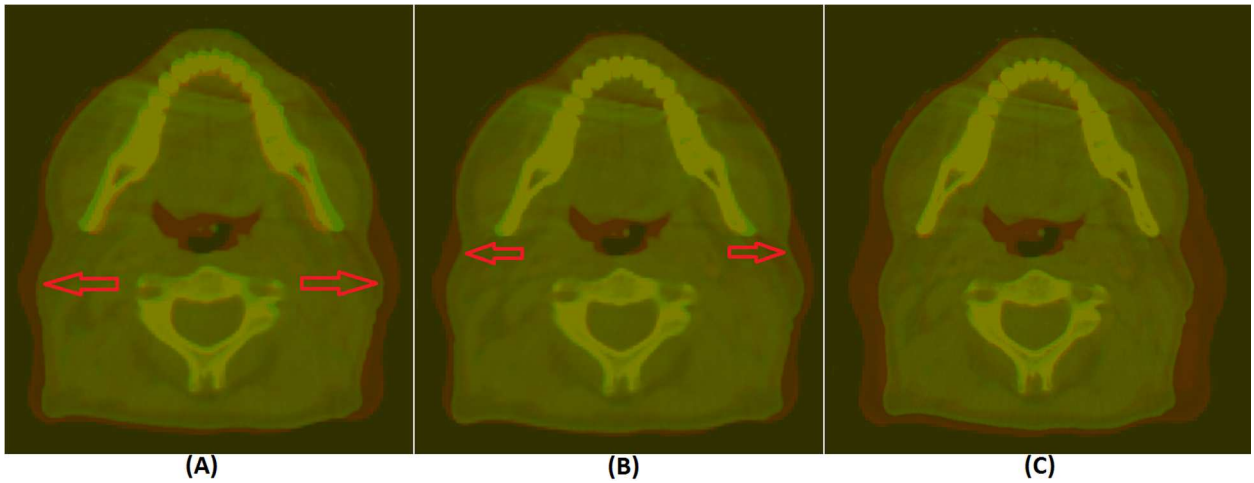

Figure 4.7 Patient 2: (A) pCT (red) overlaid on the resampled CBCT of the last treatment fraction. CBCT is resampled using the diffeomorphic demons DVF compressed with the factor 7; (B) pCT (red) overlaid on the epCT (green). Red arrows show the underestimation of the parotids movement due to the large CF used for the DVFs; (C) pCT (red) overlaid on the last fraction CBCT (green).

Figures 4.8, 4.9 and 4.10 show the results of the movement underestimation of the patients anatomy by the DVFs by comparing the planned (blue) and modeled (green and brown) DVHs presented above with the "real" accumulated DVH (red) for the left and right parotids, and spinal cord.

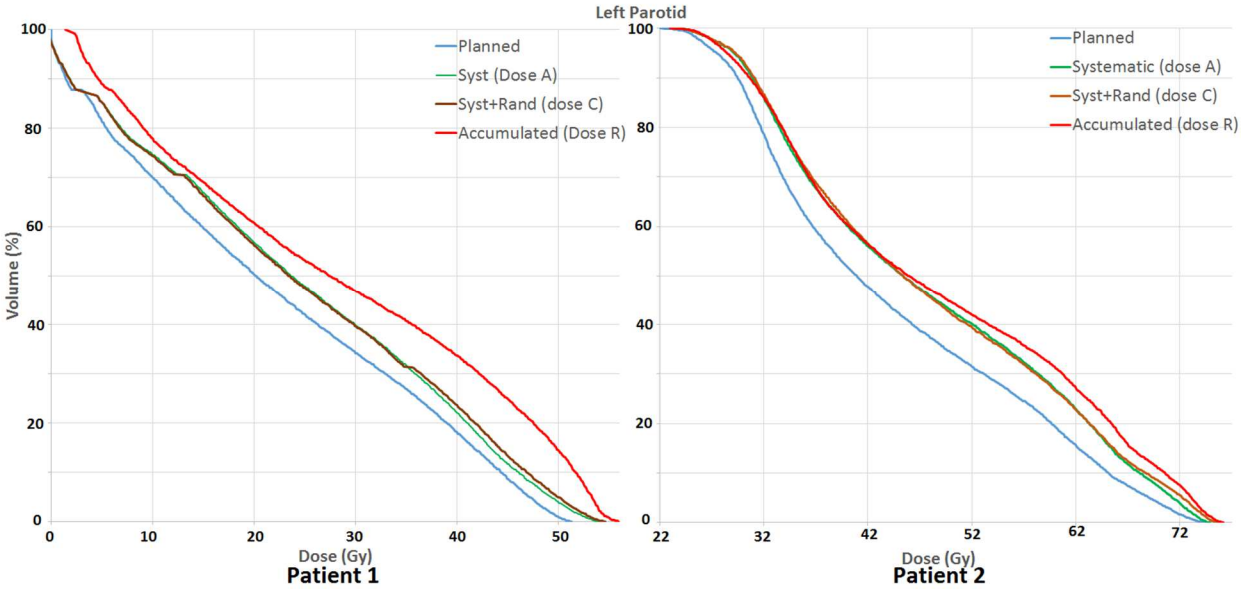

Figure 4.8 Patients 1 and 2: Comparison of the planned DVHs (blue) for the left parotid glands vs. the simulated DVHs (green, brown) vs. "real" cumulative DVH.

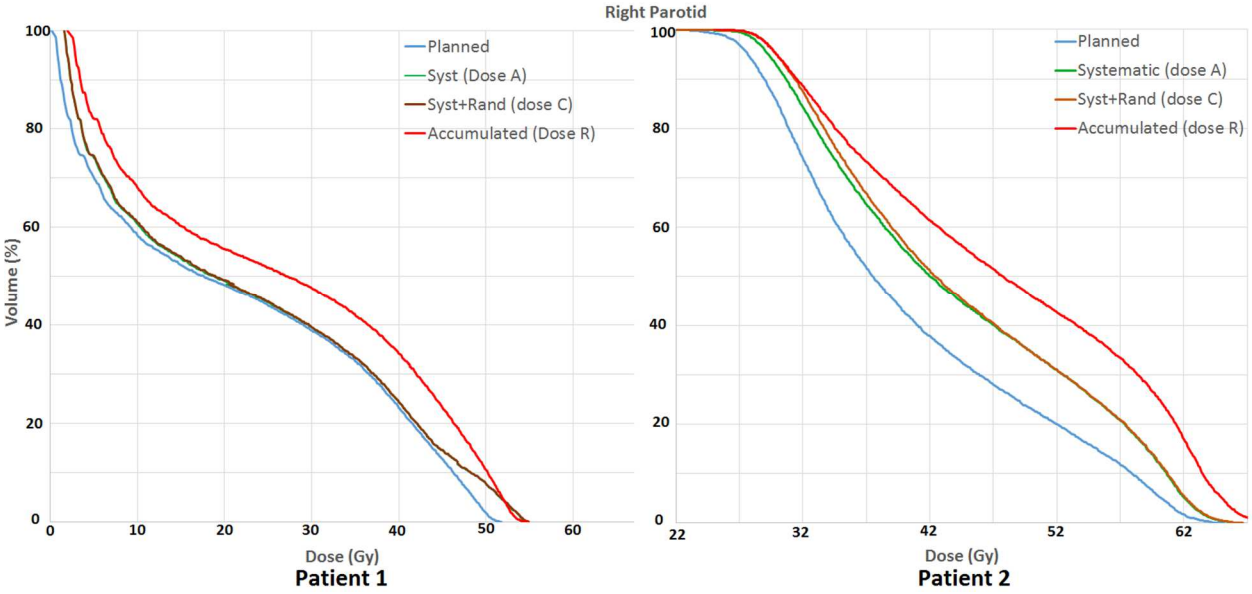

Figure 4.9 Patients 1 and 2: Comparison of the planned DVHs (blue) for the right parotid glands vs. the simulated DVHs (green, brown) vs. "real" cumulative DVH.

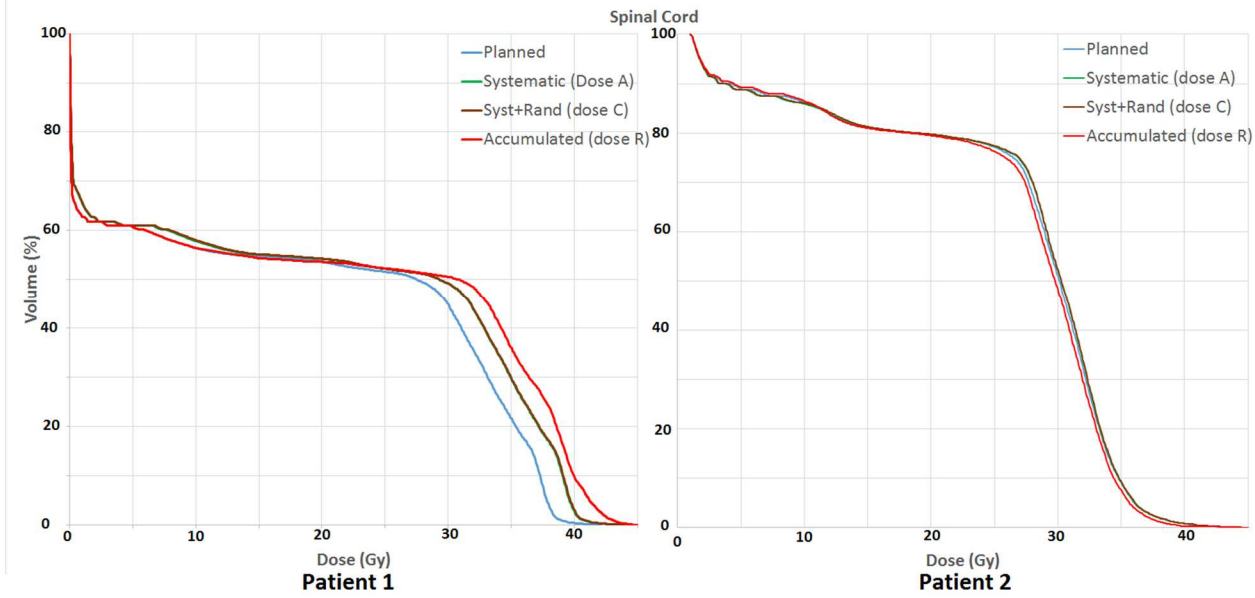

Figure 4.10 Patients 1 and 2: Comparison of the planned DVHs (blue) for the spinal cords vs. the simulated DVHs (green, brown) vs. "real" cumulative DVH.

Table 4.1 summarizes the cumulative dosimetric parameters of the OARs for both patients 1 and 2. Mean and maximum doses for the parotid glands, and maximum dose for the spinal cord are compared between planned, simulated (using both systematic and random components), modeled (using both systematic and random

components) and cumulative cases. The relative difference from the planned dose (equation 4.1) is presented in parentheses.

			Patient 1		Patient 2	
			D_{mean}	D_{max}	D_{mean}	D_{max}
Left parotid	*Planned*		23.5	51.0	44.6	74.4
	Simulated, dose C		25.1 (6.8%)	54.1 (6.1%)	49.8 (11.7%)	75.9 (2.0%)
	Modeled, dose D	*5fx*	23.7 (0.9%)	52.5 (2.9%)	46.6 (4.5%)	74.9 (0.7%)
		Half	25.1 (6.8%)	53.9 (5.7%)	49.3 (10.5%)	75.6 (1.6%)
		All	25.7 (9.4%)	54.3 (6.5%)	50.5 (13.2%)	75.7 (1.7%)
	Cumulative		27.0 (14.9%)	55.9 (9.6%)	52.5 (17.7%)	76.6 (3.0%)
Right Parotid	*Planned*		23.0	51.8	41.7	65.2
	Simulated, dose C		24.5 (6.5%)	54.3 (4.8%)	47.9 (14.9%)	67.9 (4.1%)
	Modeled, dose D	*5fx*	23.5 (2.2%)	51.0 (-1.5%)	44.5 (6.7%)	66.3 (1.7%)
		Half	24.9 (8.3%)	54.8 (5.8%)	47.1 (12.9%)	67.8 (4.0%)
		All	24.4 (6.1%)	54.3 (4.8%)	48.6 (16.5%)	68.7 (5.4%)
	Cumulative		25.7 (11.7%)	55.1 (6.4%)	50.1 (20.1%)	69.8 (7.1%)
			D_{max}		D_{max}	
Spinal Cord	*Planned*		42.1		45.2	
	Simulated, dose C		43.9 (4.3%)		45.2 (0%)	
	Modeled,	*5fx*	42.9 (1.9%)		44.9 (-0.7%)	
		Half	43.3 (2.9%)		45.3 (0.2%)	
		All	43.5 (3.3%)		45.3 (0.2%)	
	Cumulative		45.2 (7.4%)		45.4 (0.4%)	

Table 4.1 Planned, simulated, modeled and accumulated dosimetric parameters for the patients (in Gy). The relative percentage difference from the planned dose presented in parentheses.

Discussion

Figures 4.1, 4.3 and 4.5 show the DVHs for the simulated and modeled left parotid, right parotid and spinal cord respectively when only systematic changes are introduced in patients 1 and 2 with parotid shrinkage, and parotid shrinkage and weight loss as a major mode of anatomical change during radiation therapy, respectively. These are compared to the planned DVH. It can be seen qualitatively that the planned dose to the parotids is different from the simulated (Figures 4.1, 4.3, dose A) and modeled doses (Figures 4.1, 4.3, dose B). Due to the shrinkage, the parotids are shifted into the area of higher dose and accumulate more dose than was planned. However, changes in the parotids did not affect the movement of the spinal cord of the patient 2 during the radiation therapy course, and the dose to the spinal cord didn't change for the simulated course compared to the planning course. On the other hand, as shown in Table 4.1, patient 1 experienced dose escalation from the planned (42.1Gy) to simulated (45.2Gy) treatment course. While in this case this unintended 3 Gy increase in the dose to a critical OAR would likely be acceptable[24], this is not always the case. For example, if the modeled maximum dose to the spinal cord had been 55 Gy, additional dose in such case would predict a substantial increase in Normal Tissue Complication Probability (NTCP).

For the patients 1 and 2, RPCA anatomy modeling when using DVFs from the first 5 fractions qualitatively showed larger deviation from the simulated treatment course for the parotids, especially in the areas of higher doses (Figures 4.1, 4.3). RPCA models when using DVFs from the half and all-but-last fraction show good conformity with the simulated treatment course. This means that when using enough data for building the model, RPCA can identify and capture the major mode of anatomical change and it can

be used to model the anatomy of the future fractions. For the case of the spinal cord the planned, simulated (dose A), and modeled (doses B) DVHs didn't show much qualitative (Figure 4.5) or quantitative (Table 4.1) difference compared to the parotid glands for patient 2. For patient 1, the DVHs show an increase in dose for both simulated (dose A) and modeled (doses B) cases. The results in figures 4.1, 4.3, 4.5 and Table 4.1 support the hypothesis *H1*, which means that RPCA models can quantify deviations between planned and delivered cumulative dose caused by systematic anatomical changes given sufficient patient data to enable extraction of mean trends in the presence of random background.

Figures 4.2, 4.4 and 4.6 show the DVHs for the simulated (dose C) and modeled (doses D) left parotid, right parotid and spinal cord respectively when systematic and random changes are introduced in the patients 1 and 2. These are compared to the planned DVHs. As demonstrated above, qualitatively the planned dose to the parotids is different from the simulated (Figures 4.2, 4.4, dose C) and modeled ones (Figures 4.2, 4.4, dose D). Quantitative differences between these doses are presented in Table 4.1. Similarly to the case with only systematic changes applied, due to the shrinkage, the parotids are shifted into the area of the higher dose and accumulate more dose than was planned. Even when random changes are introduced to the patients 1 and 2, this did not affect the movement of the spinal cord in patient 2 during the radiation therapy course, and the dose to the spinal cord of the patient 2 didn't change (Table 4.1) for the simulated course compared to the planning course. This means that even in the presence of noise, RPCA is able to differentiate it from the systematic anatomical changes and such random changes are mostly ignored by the model due to the use of the sparseness parameter τ_2.

RPCA anatomy modeling when using DVFs from the first 5 fractions showed larger deviation from the simulated treatment course for both parotids (Figures 4.2, 4.4, Table 4.1), especially in the areas of higher doses. But RPCA models built using DVFs from the half and all-but-last fraction show good conformity with the simulated treatment course. That also means that RPCA can identify and capture the major mode of anatomical change even in the presence of the random changes and it can be used to model the anatomy of the future fractions. For the spinal cord of the patient 1 (Figure 4.6), planned, simulated (dose C) and modeled (doses D) showed the difference of up to 3.3% (Table 4.1) from the planned DVH. For the spinal cord of the patient 2 (Figure 4.6), planned, simulated (dose C) and modeled (doses D) DVHs didn't show much difference (<1%, Table 4.1) from planned DVH compared to the parotid glands. The results in figures 4.2, 4.4 and 4.6 support the hypothesis *H2*, which means that RPCA models can quantify deviations between planned and delivered cumulative dose caused by both systematic and random anatomical changes.

The RPCA models in this work used DVFs acquired using a large CF value (7), and using such compressed DVFs usually underestimates the anatomical changes present in the patients. Figure 4.7 (A) shows the pCT image (red) overlaid on the resampled CBCT image of the last treatment fraction. CBCT is resampled using the diffeomorphic demons DVF compressed with a factor of 7. Figure 4.7 (B) shows the pCT image (red) overlaid on the epCT (green) of the patient. Figure 4.7 (C) shows the pCT image (red) overlaid on the last fraction CBCT image (green). Ideally, it is expected that pCT and epCT images would be exactly the same, but as can be seen in Figure 4.7 (B), motion of the parotids is underestimated by the model due to the large CF of the DVFs.

Such effects are not only seen on the epCT image acquired from the modeled DVFs, but also on resampled last fraction CBCT image acquired using real clinical DVFs compressed with the same CF, as seen on Figure 4.7 (A). This means that even though RPCA could capture the correct major mode of anatomical changes in the patient from compressed DVFs, it is possible that these changes would be underestimated and the model will show less movement in the anatomy than in the real case. Another challenge of using the compressed DVFs is that they can't capture the movement on a "wiggly" edge, like those on the parotids in Figure 4.7. So using a large CF will suppress the smaller and "wigglier" anatomical changes in the DVFs, and therefore RPCA would not be able to extract such changes form this dataset. In general, the quality of the RPCA models is dependent on the quality of the input data, the DVFs.

Such underestimation of the anatomical changes could lead to the underestimation of the dose distribution changes in the patient. This effect is shown for the parotids and spinal cords of the patients 1 and 2 on Figures 4.8, 4.9 and 4.10. On these figures, planned DVH (blue) is compared to the simulated DVH, acquired from the anatomy resampled with the compressed DVFs (green, brown), and in turn compared to the "real" accumulated DVH (red) for the patient. As can be seen, the "real" DVH is shifted to the right with respect to the modeled DVHs. This means that underestimation of the parotid shrinkage in the modeled cases leads to the underestimation of the dose received by parotids due to their shift into the high dose region.

Based on the visual examination of the performance of the compressed DVFs (Figure 4.7), and subsequent dosimetric DVHs' deviations calculated based on these corresponding DVFs (Table 4.1), future work on RPCA models requires use of DVFs with

smaller CF in order to capture smaller changes in the anatomy.

Conclusion

This work showed that RPCA has the potential to identify the major mode of anatomical changes during the radiotherapy course in which allows the prediction of dose for the course of treatment. There are some challenges presented with the DVFs compressed using a large CF, so use of smaller CF should be considered for the future work. There is a hope, that using RPCA modeling could provide a roadmap for how to use PCA in ART: (i) RPCA models are generated based on initial fractions, (ii) dose deviations due to underlying systematic change are projected for future fractions to trigger re-planning decisions, (iii) effects of random changes are superimposed to guide what margins should be used.

CHAPTER 5 "CONCLUSIONS AND FUTURE WORK"

Summary of Findings

As discussed in Chapter 1, the modeling of anatomical changes over the course of head-and-neck treatment is essential to answer practical questions such as: What anatomical changes are important? How do we measure them? When to trigger re-planning? And how best to perform the re-planning? Such models should take into account not only rigid body transformations but also deformations, and be capable of extracting useful information about changes in patient anatomy, ideally early in the radiation treatment course.

PCA was chosen as a core element of this work because of its use in developing motion models of anatomical changes during the radiation therapy course. PCA has been used in many previous applications, specifically in the field of radiation therapy[47, 49-52]. However, the implementation of PCA models has not been utilized for extracting systematic changes in patient anatomy during a H&N radiation therapy course.

Two approaches to the PCA were implemented: a standard approach to PCA (SPCA, Chapter 2) and a more advanced regularized approach (RPCA, Chapter 3).

The results showed that for the H&N patients treated with external beam radiation therapy included in this cohort, a SPCA model was a potential tool for identifying patient anatomy changes early in the treatment course, and making educated adaptive re-planning decisions. The study showed that under the right conditions, SPCA can capture the major mode of systematic anatomical deformation in the leading EDVF. However, SPCA is most successful at identify large changes (e.g., significant lymph node

shrinkage), and less successful at identifying small changes (e.g., smaller changes in parotid glands). Additionally, SPCA is challenged by the variety of deformations and noise in clinical CBCT images, and therefore fails to extract major modes of systematic change that are known to be present.

In order to successfully model anatomical changes in clinical CBCT images, the basic SPCA technique has been refined using a regularized approach to the PCA, RPCA (Chapter 3). Using a regularized approach, we have shown that the RPCA model is a potential tool for identifying patient anatomy changes early in the treatment course. In contrast to SPCA, the RPCA approach was able to identify smaller changes compared to the random fraction-to-fraction changes. The drawback of the RPCA approach is the time necessary for the calculation, memory requirements and use of large CF for the DVFs.

The dosimetric study (Chapter 4) showed that PCA models have the potential to identify the major mode of anatomical changes during the radiotherapy course which allow the prediction of dose for the treatment course. There were some challenges presented with the DVFs compressed using a large CF, so using smaller CF should be considered in future work. In summary, the work presented provides direction for the implementation of RPCA modeling in ART.

Future Work

One of the main directions of the current research going forward is the accumulation of the H&N patient datasets in order to create population-based models of anatomical changes. Population based models will be generated from large numbers of patients, and should therefore capture modes of anatomical change that apply to most

patients, even if the relative weighting of those modes differs across individuals. Population-based models should therefore provide a good starting point for predicting anatomical changes that are expected during the course of treatment, for the majority of patients. For many patients, it may be necessary to make only minor changes to the population model, in order to model the patient-specific anatomical change.

For patients who do not fall into the above category, projection of early fractions onto the population-based EDVFs should allow one to detect significant deviations from the population-based model. That is, it should allow one to identify the minority of 'outlier' patients whose major modes of anatomical change differ significantly from the majority of patients. This in turn will trigger one to develop a patient-specific model, and carefully model changes within outlier patients, for unexpected dosimetric consequences. Population-based models will be useful for triggering customized treatment strategies for outlier patients.

DVFs which are used as an input for the PCA define an overall quality of the model. It has been showed in Chapter 4 that using DVFs with large CF could underestimate the effects of anatomy motion in the patients, and moreover limit the ability to detect the movement on "wiggly" edges. Therefore PCA also is unable to detect such changes, which potentially could be important. So, in the future, the use of less compressed or non-compressed DVFs should be considered. The regularized approach requires a calculation of very large penalty matrices which in turn requires a lot of time, so the compromise between DVF's CF and time of calculation should be found. The hope is that with further advancement in computing technologies, calculations of such large datasets will be faster and cheaper.

The quality of the DIR is also closely related to the quality of the PCA models. DVF accuracies have an impact on the accuracies of PCA models, but one can reasonably hope that RPCA models will be insensitive to small scale uncertainties present in DVFs, and instead extract larger scale anatomical changes corresponding to observable clinical change. Even though checking the quality of the DIR was not an aim of this work, using different DIR algorithms with different parameters and assessing their effects on the quality of the PCA models should be considered in future studies.

Another area of the research pertains to improving RPCA, particularly in optimizing the smoothness (τ_1) and sparseness (τ_2) parameters, while solving the constrained optimization problem (equation 3.1). In this work these parameters were optimized empirically with the assumption that sparseness parameter should have a larger weight than the smoothness parameters due to intrinsic smoothness of the DVFs acquired with the large CF. However, future work should include further study of these parameters in order to find which ones are optimal, especially in light of population-based model developments.

APPENDIX

STANDARD PRINCIPAL COMPONENT ANALYSIS MATRIX OPERATIONS

Each column in a set of DVFs $\boldsymbol{D} = [D_1, \dots, D_F]$ form a vector $D_i \in R^{3M}$, where *i* is the treatment fraction number, and M is the number of voxel elements in DVF. Each DVF (column) could be represented as follows:

$$D_i = (x_{1,i}, x_{2,i}, \dots, x_{M,i}, y_{1,i}, y_{2,i}, \dots, y_{M,i}, z_{1,i}, z_{2,i}, \dots, z_{M,i})^T \quad \text{(A.1)}$$

where x, y, and z are the displacement vector field components in each direction for each DVF voxel, and $()^T$ is denoted the transpose of the vector, making it 3M x 1 DVF vector.

Each vector D_i then could be composed into a matrix $\boldsymbol{D}(n) \in R^{3M \times n}$, where n corresponds to a number of initial treatment fractions used for PCA analysis, with the minimum of 2 initial fraction, and a maximum of the whole number of fractions, i.e. 35, or *n=2÷35*:

$$\boldsymbol{D}(n) = (D_1, D_2, \dots, D_n) \quad \text{(A.2)}$$

The PCA analysis and predictive model is built using this $\boldsymbol{D}(n)$ matrix.

The larger the number of treatment fractions n used as input data for PCA, the larger the chance that the model could capture systematic changes in the patient. Therefore, one faces an important trade-off here: the purpose of the model is to reliably capture systematic changes, which is more likely when the number *n* of treatment fractions used to build a model is high, but the other purpose is to capture these changes early enough, so ART can still be applied to that patient.

Covariance matrix for $\boldsymbol{D}(n)$ represented as:

$$\boldsymbol{C} = \frac{1}{n}\boldsymbol{D}(n)\boldsymbol{D}(n)^T \quad \text{(A.3)}$$

which generalizes the variance to 3M x 3M dimension. Determining 3M

eigenvalues and 3M corresponding eigenvectors is a complex, intractable and, after all, unnecessary task. There are computationally more feasible and much faster methods to find these. This alternative method is useful when the number of measurements is much less than number of dimensions, or n<<M.

First, substitute A.3 into the eigenvector equation:

$$\frac{1}{n}\boldsymbol{D}(n)\boldsymbol{D}(n)^T\boldsymbol{V}(n) = \lambda\boldsymbol{V}(n) \qquad \text{(A.4)}$$

$\boldsymbol{V}(n)$ represent eigenvectors for the covariance matrix **C**, and λ are the corresponding eigenvalues.

Multiplying both sides of A.4 by $\boldsymbol{D}(n)^T$ and defining $\boldsymbol{U}(n) = \boldsymbol{D}(n)^T\boldsymbol{V}(n)$ gives us:

$$\frac{1}{n}\boldsymbol{D}(n)^T\boldsymbol{D}(n)\boldsymbol{U}(n) = \lambda\boldsymbol{U}(n) \qquad \text{(A.5)}$$

A.5 is a reformed equation which gives us eigenvalues and eigenvectors of smaller matrix of the size *n x n*: $\boldsymbol{D}(n)^T\boldsymbol{D}(n)$.

Multiplying both sides of A.5 by $\boldsymbol{D}(n)$:

$$\frac{1}{n}\boldsymbol{D}(n)\boldsymbol{D}(n)^T(\boldsymbol{D}(n)\boldsymbol{U}(n)) = \lambda(\boldsymbol{D}(n)\boldsymbol{U}(n)) \qquad \text{(A.6)}$$

Thus from A.5 it follows that eigenvectors for the covariance matrix **C** defined in A.3:

$$\boldsymbol{V}_i(n) = \frac{1}{\sqrt{\lambda_i n}}\boldsymbol{D}(n)\boldsymbol{U}_i(n) \qquad \text{(A.7)}$$

Where the factor $\frac{1}{\sqrt{\lambda_i n}}$ is used to renormalize the eigenvector $\boldsymbol{V}_i(n)$, such as $\|\boldsymbol{V}_i(n)\| = 1$.

These eigenvectors $\boldsymbol{V}_i(n)$ are defined as EDVFs in this work and they represent mutually independent vector fields with the maximum number of meaningful EDVFs n-1 (one of the EDVFs corresponds to the zero eigenvalue and is not meaningful).

Thus, the matrix of meaningful EDVFs has the form $\boldsymbol{V}(n) \in \boldsymbol{R}^{\boldsymbol{3M}\times(\boldsymbol{n-1})}$, where each column represents each $EDVF_i$, and the $EDVF_1$ corresponds to the largest eigenvalue positioned at the first column of $\boldsymbol{V}(n)$, the $EDVF_2$ corresponds to the second largest eigenvalue, etc.

REFERENCES

1 J.M. Wilkinson, "Geometric uncertainties in radiotherapy," Br J Radiol **77**, 86-87 (2004).

2 C.W. Hurkmans, P. Remeijer, J.V. Lebesque, B.J. Mijnheer, "Set-up verification using portal imaging; review of current clinical practice," Radiother Oncol **58**, 105-120 (2001).

3 C.S. Chui, E. Yorke, L. Hong, "The effects of intra-fraction organ motion on the delivery of intensity-modulated field with a multileaf collimator," Med Phys **30**, 1736-1746 (2003).

4 S. Webb, "Motion effects in (intensity modulated) radiation therapy: a review," Phys Med Biol **51**, R403-425 (2006).

5 R. Varadhan, S.K. Hui, S. Way, K. Nisi, "Assessing prostate, bladder and rectal doses during image guided radiation therapy--need for plan adaptation?," J Appl Clin Med Phys **10**, 2883 (2009).

6 Z. Gao, D. Wilkins, L. Eapen, C. Morash, Y. Wassef, L. Gerig, "A study of prostate delineation referenced against a gold standard created from the visible human data," Radiother Oncol **85**, 239-246 (2007).

7 C.F. Njeh, "Tumor delineation: The weakest link in the search for accuracy in radiotherapy," J Med Phys **33**, 136-140 (2008).

8 C. Rasch, R. Steenbakkers, M. van Herk, "Target definition in prostate, head, and neck," Semin Radiat Oncol **15**, 136-145 (2005).

9 A. Isambert, F. Dhermain, F. Bidault, O. Commowick, P.Y. Bondiau, G. Malandain, D. Lefkopoulos, "Evaluation of an atlas-based automatic segmentation software

for the delineation of brain organs at risk in a radiation therapy clinical context," Radiother Oncol **87**, 93-99 (2008).

[10] J.L. Barker, Jr., A.S. Garden, K.K. Ang, J.C. O'Daniel, H. Wang, L.E. Court, W.H. Morrison, D.I. Rosenthal, K.S. Chao, S.L. Tucker, R. Mohan, L. Dong, "Quantification of volumetric and geometric changes occurring during fractionated radiotherapy for head-and-neck cancer using an integrated CT/linear accelerator system," Int J Radiat Oncol Biol Phys **59**, 960-970 (2004).

[11] P. Castadot, X. Geets, J.A. Lee, N. Christian, V. Gregoire, "Assessment by a deformable registration method of the volumetric and positional changes of target volumes and organs at risk in pharyngo-laryngeal tumors treated with concomitant chemo-radiation," Radiother Oncol **95**, 209-217 (2010).

[12] J.D. Chencharick, K.L. Mossman, "Nutritional consequences of the radiotherapy of head and neck cancer," Cancer **51**, 811-815 (1983).

[13] S.S. Donaldson, R.A. Lenon, "Alterations of nutritional status: impact of chemotherapy and radiation therapy," Cancer **43**, 2036-2052 (1979).

[14] C. Lee, K.M. Langen, W. Lu, J. Haimerl, E. Schnarr, K.J. Ruchala, G.H. Olivera, S.L. Meeks, P.A. Kupelian, T.D. Shellenberger, R.R. Manon, "Evaluation of geometric changes of parotid glands during head and neck cancer radiotherapy using daily MVCT and automatic deformable registration," Radiother Oncol **89**, 81-88 (2008).

[15] "ICRU Report 50—Prescribing, Recording and Reporting Photon Beam Therapy | Browse - Medical Physics," 1994).

16 "ICRU Report 62 - Prescribing, Recording and Reporting Photon Beam Therapy (Supplement to ICRU Report 50)," 2000).

17 M. van Herk, P. Remeijer, J.V. Lebesque, "Inclusion of geometric uncertainties in treatment plan evaluation," Int J Radiat Oncol Biol Phys **52**, 1407-1422 (2002).

18 M.R. Button, C.A. Morgan, E.S. Croydon, S.A. Roberts, T.D. Crosby, "Study to determine adequate margins in radiotherapy planning for esophageal carcinoma by detailing patterns of recurrence after definitive chemoradiotherapy," Int J Radiat Oncol Biol Phys **73**, 818-823 (2009).

19 L. Ekberg, O. Holmberg, L. Wittgren, G. Bjelkengren, T. Landberg, "What margins should be added to the clinical target volume in radiotherapy treatment planning for lung cancer?," Radiother Oncol **48**, 71-77 (1998).

20 S.W. Lee, B.A. Fraass, L.H. Marsh, K. Herbort, S.S. Gebarski, M.K. Martel, E.H. Radany, A.S. Lichter, H.M. Sandler, "Patterns of failure following high-dose 3-D conformal radiotherapy for high-grade astrocytomas: a quantitative dosimetric study," Int J Radiat Oncol Biol Phys **43**, 79-88 (1999).

21 L.P. Muren, R. Smaaland, O. Dahl, "Organ motion, set-up variation and treatment margins in radical radiotherapy of urinary bladder cancer," Radiother Oncol **69**, 291-304 (2003).

22 M. van Herk, P. Remeijer, C. Rasch, J.V. Lebesque, "The probability of correct target dosage: dose-population histograms for deriving treatment margins in radiotherapy," Int J Radiat Oncol Biol Phys **47**, 1121-1135 (2000).

23 J.C. Stroom, B.J. Heijmen, "Limitations of the planning organ at risk volume (PRV) concept," Int J Radiat Oncol Biol Phys **66**, 279-286 (2006).

[24] L.B. Marks, E.D. Yorke, A. Jackson, R.K. Ten Haken, L.S. Constine, A. Eisbruch, S.M. Bentzen, J. Nam, J.O. Deasy, "Use of Normal Tissue Complication Probability Models in the Clinic," Int J Radiat Oncol **76**, S10-S19 (2010).

[25] D.A. Jaffray, P.E. Lindsay, K.K. Brock, J.O. Deasy, W.A. Tome, "Accurate accumulation of dose for improved understanding of radiation effects in normal tissue," Int J Radiat Oncol Biol Phys **76**, S135-139 (2010).

[26] L.F. Cazzaniga, M.A. Marinoni, A. Bossi, E. Bianchi, E. Cagna, D. Cosentino, L. Scandolaro, M. Valli, M. Frigerio, "Interphysician variability in defining the planning target volume in the irradiation of prostate and seminal vesicles," Radiother Oncol **47**, 293-296 (1998).

[27] C.H. Ketting, M. Austin-Seymour, I. Kalet, J. Unger, S. Hummel, J. Jacky, "Consistency of three-dimensional planning target volumes across physicians and institutions," Int J Radiat Oncol Biol Phys **37**, 445-453 (1997).

[28] H. Vorwerk, G. Beckmann, M. Bremer, M. Degen, B. Dietl, R. Fietkau, T. Gsanger, R.M. Hermann, M.K. Alfred Herrmann, U. Holler, M. van Kampen, W. Korber, B. Maier, T. Martin, M. Metz, R. Richter, B. Siekmeyer, M. Steder, D. Wagner, C.F. Hess, E. Weiss, H. Christiansen, "The delineation of target volumes for radiotherapy of lung cancer patients," Radiother Oncol **91**, 455-460 (2009).

[29] L. Xing, B. Thorndyke, E. Schreibmann, Y. Yang, T.F. Li, G.Y. Kim, G. Luxton, A. Koong, "Overview of image-guided radiation therapy," Med Dosim **31**, 91-112 (2006).

30 T. Li, X. Zhu, D. Thongphiew, W.R. Lee, Z. Vujaskovic, Q. Wu, F.F. Yin, Q.J. Wu, "On-line adaptive radiation therapy: feasibility and clinical study," J Oncol **2010**, 407236 (2010).

31 D. Yan, F. Vicini, J. Wong, A. Martinez, "Adaptive radiation therapy," Phys Med Biol **42**, 123-132 (1997).

32 K.S. Chao, D.A. Low, C.A. Perez, J.A. Purdy, "Intensity-modulated radiation therapy in head and neck cancers: The Mallinckrodt experience," Int J Cancer **90**, 92-103 (2000).

33 K.S. Chao, G. Ozyigit, B.N. Tran, M. Cengiz, J.F. Dempsey, D.A. Low, "Patterns of failure in patients receiving definitive and postoperative IMRT for head-and-neck cancer," Int J Radiat Oncol Biol Phys **55**, 312-321 (2003).

34 A. Eisbruch, R.K. Ten Haken, H.M. Kim, L.H. Marsh, J.A. Ship, "Dose, volume, and function relationships in parotid salivary glands following conformal and intensity-modulated irradiation of head and neck cancer," Int J Radiat Oncol Biol Phys **45**, 577-587 (1999).

35 N. Lee, P. Xia, N.J. Fischbein, P. Akazawa, C. Akazawa, J.M. Quivey, "Intensity-modulated radiation therapy for head-and-neck cancer: the UCSF experience focusing on target volume delineation," Int J Radiat Oncol Biol Phys **57**, 49-60 (2003).

36 C. Han, Y.J. Chen, A. Liu, T.E. Schultheiss, J.Y. Wong, "Actual dose variation of parotid glands and spinal cord for nasopharyngeal cancer patients during radiotherapy," Int J Radiat Oncol Biol Phys **70**, 1256-1262 (2008).

[37] J.C. O'Daniel, A.S. Garden, D.L. Schwartz, H. Wang, K.K. Ang, A. Ahamad, D.I. Rosenthal, W.H. Morrison, J.A. Asper, L. Zhang, S.M. Tung, R. Mohan, L. Dong, "Parotid gland dose in intensity-modulated radiotherapy for head and neck cancer: is what you plan what you get?," Int J Radiat Oncol Biol Phys **69**, 1290-1296 (2007).

[38] J. Wang, S. Bai, N. Chen, F. Xu, X. Jiang, Y. Li, Q. Xu, Y. Shen, H. Zhang, Y. Gong, R. Zhong, Q. Jiang, "The clinical feasibility and effect of online cone beam computer tomography-guided intensity-modulated radiotherapy for nasopharyngeal cancer," Radiother Oncol **90**, 221-227 (2009).

[39] D.L. Schwartz, A.S. Garden, S.J. Shah, G. Chronowski, S. Sejpal, D.I. Rosenthal, Y. Chen, Y. Zhang, L. Zhang, P.F. Wong, J.A. Garcia, K. Kian Ang, L. Dong, "Adaptive radiotherapy for head and neck cancer--dosimetric results from a prospective clinical trial," Radiother Oncol **106**, 80-84 (2013).

[40] E. Budiarto, M. Keijzer, P.R. Storchi, M.S. Hoogeman, L. Bondar, T.F. Mutanga, H.C. de Boer, A.W. Heemink, "A population-based model to describe geometrical uncertainties in radiotherapy: applied to prostate cases," Phys Med Biol **56**, 1045-1061 (2011).

[41] E. Fontenla, C.A. Pelizzari, J.C. Roeske, G.T. Chen, "Using serial imaging data to model variabilities in organ position and shape during radiotherapy," Phys Med Biol **46**, 2317-2336 (2001).

[42] M.S. Hoogeman, M. van Herk, D. Yan, L.J. Boersma, P.C. Koper, J.V. Lebesque, "A model to simulate day-to-day variations in rectum shape," Int J Radiat Oncol Biol Phys **54**, 615-625 (2002).

[43] G.S. Mageras, G.J. Kutcher, S.A. Leibel, M.J. Zelefsky, E. Melian, R. Mohan, Z. Fuks, "A method of incorporating organ motion uncertainties into three-dimensional conformal treatment plans," Int J Radiat Oncol Biol Phys **35**, 333-342 (1996).

[44] T.F. Mutanga, H.C. de Boer, G.J. van der Wielen, M.S. Hoogeman, L. Incrocci, B.J. Heijmen, "Margin evaluation in the presence of deformation, rotation, and translation in prostate and entire seminal vesicle irradiation with daily marker-based setup corrections," Int J Radiat Oncol Biol Phys **81**, 1160-1167 (2011).

[45] M. Sohn, M. Birkner, D. Yan, M. Alber, "Modelling individual geometric variation based on dominant eigenmodes of organ deformation: implementation and evaluation," Phys Med Biol **50**, 5893-5908 (2005).

[46] D. Yan, D.A. Jaffray, J.W. Wong, "A model to accumulate fractionated dose in a deforming organ," Int J Radiat Oncol Biol Phys **44**, 665-675 (1999).

[47] M. Sohn, B. Sobotta, M. Alber, "Dosimetric treatment course simulation based on a statistical model of deformable organ motion," Phys Med Biol **57**, 3693-3709 (2012).

[48] I.T. Jolliffe, *Principal component analysis*, 2nd ed. (Springer, New York, 2002).

[49] G.J. Price, C.J. Moore, "A method to calculate coverage probability from uncertainties in radiotherapy via a statistical shape model," Phys Med Biol **52**, 1947-1965 (2007).

[50] Q. Zhang, A. Pevsner, A. Hertanto, Y.C. Hu, K.E. Rosenzweig, C.C. Ling, G.S. Mageras, "A patient-specific respiratory model of anatomical motion for radiation treatment planning," Med Phys **34**, 4772-4781 (2007).

[51] V. Pekar, T.R. McNutt, M.R. Kaus, "Automated model-based organ delineation for radiotherapy planning in prostatic region," Int J Radiat Oncol Biol Phys **60**, 973-980 (2004).

[52] D. Merck, G. Tracton, R. Saboo, J. Levy, E. Chaney, S. Pizer, S. Joshi, "Training models of anatomic shape variability," Med Phys **35**, 3584-3596 (2008).

[53] K. Pearson, "LIII. On lines and planes of closest fit to systems of points in space," Philosophical Magazine Series 6 **2**, 559-572 (1901).

[54] K.T. Gribbon, C.T. Johnston, D.G. Bailey, *A Real-time FPGA Implementation of a Barrel Distortion Correction Algorithm with Bilinear Interpolation*.

[55] GNU Scientific Library - GNU Project - Free Software Foundation, http://www.gnu.org/software/gsl/

[56] J.P. Thirion, presented at the Computer Vision and Pattern Recognition, 1996. Proceedings CVPR '96, 1996 IEEE Computer Society Conference on1996 (unpublished).

[57] T. Vercauteren, X. Pennec, A. Perchant, N. Ayache, "Non-parametric Diffeomorphic Image Registration with the Demons Algorithm," in *Medical Image Computing and Computer-Assisted Intervention – MICCAI 2007: 10th International Conference, Brisbane, Australia, October 29 - November 2, 2007, Proceedings, Part II,* edited by N. Ayache, S. Ourselin, A. Maeder (Springer Berlin Heidelberg, Berlin, Heidelberg, 2007), pp. 319-326.

[58] T. Vercauteren, X. Pennec, A. Perchant, N. Ayache, "Diffeomorphic demons: efficient non-parametric image registration," NeuroImage **45**, S61-72 (2009).

[59] D. Yang, S. Brame, I. El Naqa, A. Aditya, Y. Wu, S.M. Goddu, S. Mutic, J.O. Deasy, D.A. Low, "Technical note: DIRART--A software suite for deformable image registration and adaptive radiotherapy research," Med Phys **38**, 67-77 (2011).

[60] D.A. Low, W.B. Harms, S. Mutic, J.A. Purdy, "A technique for the quantitative evaluation of dose distributions," Med Phys **25**, 656-661 (1998).

[61] W.-T. Wang, H.-C. Huang, "Regularized Principal Component Analysis for Spatial Data," in *ArXiv e-prints*, *Vol. 1501* (2015).

[62] H. Xu, D.J. Vile, M. Sharma, J.J. Gordon, J.V. Siebers, "Coverage-based treatment planning to accommodate deformable organ variations in prostate cancer treatment," Med Phys **41**, 101705 (2014).

[63] X. Nie, J. Liang, D. Yan, "Organ sample generator for expected treatment dose construction and adaptive inverse planning optimization," Med Phys **39**, 7329-7337 (2012).

[64] D.L. Schwartz, "Current progress in adaptive radiation therapy for head and neck cancer," Curr Oncol Rep **14**, 139-147 (2012).

[65] C. Veiga, J. McClelland, S. Moinuddin, A. Lourenco, K. Ricketts, J. Annkah, M. Modat, S. Ourselin, D. D'Souza, G. Royle, "Toward adaptive radiotherapy for head and neck patients: Feasibility study on using CT-to-CBCT deformable registration for "dose of the day" calculations," Med Phys **41**, 031703 (2014).

[66] ITK - Insight Segmentation and Registration Toolkit, https://itk.org/

[67] A. Kumarasiri, C. Liu, F. Siddiqui, H. Zhong, I.J. Chetty, J. Kim, "Target and organ dose estimation from intensity modulated head and neck radiation therapy using 3 deformable image registration algorithms," Pract Radiat Oncol **5**, e317-325 (2015).

ABSTRACT

PCA-BASED ANATOMICAL MOTION MODELS FOR USING IN ADAPTIVE RADIATION THERAPY OF HEAD AND NECK CANCER PATIENTS

by

MIKHAIL A. CHETVERTKOV

August 2016

Advisor: Dr. Indrin J. Chetty

Major: Medical Physics

Degree: Doctor of Philosophy

Purpose: To develop standard and regularized principal component analysis (PCA) models of anatomical changes from daily cone beam CTs (CBCTs) of head and neck (H&N) patients, assess their potential use in adaptive radiation therapy (ART), and to extract quantitative information for treatment response assessment.

Methods: Planning CT (pCT) images of H&N patients were artificially deformed to create “digital phantom” images, which modeled systematic anatomical changes during Radiation Therapy (RT). Artificial deformations closely mirrored patients’ actual deformations, and were interpolated to generate 35 synthetic CBCTs, representing evolving anatomy over 35 fractions. Deformation vector fields (DVFs) were acquired between pCT and synthetic CBCTs (i.e., digital phantoms), and between pCT and clinical CBCTs. Patient-specific standard PCA (SPCA) and regularized PCA (RPCA) models were built from these synthetic and clinical DVF sets. Eigenvectors, or eigenDVFs (EDVFs), having the largest eigenvalues were hypothesized to capture the major

anatomical deformations during treatment. Modeled anatomies were used to assess the dose deviations with respect to the planned dose distribution.

Results: PCA models achieve variable results, depending on the size and location of anatomical change. Random changes prevent or degrade SPCA's ability to detect underlying systematic change. RPCA is able to detect smaller systematic changes against the background of random fraction-to-fraction changes, and is therefore more successful than SPCA at capturing systematic changes early in treatment. SPCA models were less successful at modeling systematic changes in clinical patient images, which contain a wider range of random motion than synthetic CBCTs, while the regularized approach was able to extract major modes of motion. For dose assessment it has been shown that the modeled dose distribution was different from the planned dose for the parotid glands due to their shrinkage and shift into the higher dose volumes during the radiotherapy course. Modeled DVHs still underestimated the effect of parotid shrinkage due to the large compression factor (CF) used to acquire DVFs.

Conclusion: Leading EDVFs from both PCA approaches have the potential to capture systematic anatomical changes during H&N radiotherapy when systematic changes are large enough with respect to random fraction-to-fraction changes. In all cases the RPCA approach appears to be more reliable than SPCA at capturing systematic changes, enabling dosimetric consequences to be projected to the future treatment fractions based on trends established early in a treatment course, or, potentially, based on population models. This work showed that PCA has a potential in identifying the major mode of anatomical changes during the radiotherapy course and

subsequent use of this information in future dose predictions is feasible. Use of smaller CF values for DVFs is preferred, otherwise anatomical motion will be underestimated.

AUTOBIOGRAPHICAL STATEMENT
MIKHAIL A. CHETVERTKOV

EDUCATION
2011-2016 Ph.D. Medical Physics, Wayne State University, Detroit, MI
2009-2011 Honors M.S. Physics, Moscow State University, Moscow, Russia
2005-2009 B.S. Physics, Moscow State University, Moscow, Russia

CERTIFICATION
2013 American Board of Radiology Part 1

PROFESSIONAL APPOINTMENTS
2011-2016 Graduate Research Assistant, Henry Ford Health System
Department of Radiation Oncology, Detroit, MI
2008-2011 Junior Research Scientist, Department of Atomic Physics and Quantum Theory of Collisions, Moscow State University, Moscow, Russia

ACADEMIC AND PROFESSIONAL MEMBERSHIPS
2013- American Association of Physicists in Medicine, Great Lakes Chapter
2011- American Association of Physicists in Medicine

COMMITTEE APPOINTMENTS
2015- AAPM Working Group on Student and Trainee Research: Member

PUBLICATIONS
1. **M.A. Chetvertkov**, F. Siddiqui, J. Kim, I.J. Chetty, A. Kumarasiri, C. Liu, J.J. Gordon, “Use of Regularized Principal Component Analysis to Model Anatomical Changes During Head and Neck Radiation Therapy for Treatment Adaptation and Response Assessment”, Accepted: Med. Phys. (2016).
2. C. Liu, A. Kumarasiri, M. Kamal, **M.A. Chetvertkov**, J. Gordon, H. Zhong, F. Siddiqui, I.J. Chetty, J. Kim, "*An automatic dosimetric and geometric tracking system for head and neck adaptive radiotherapy*," in World Congress on Medical Physics and Biomedical Engineering, June 7-12, 2015, Toronto, Canada, edited by A.D. Jaffray (Springer International Publishing, Cham, 2015), pp. 570-574.
3. **M.A. Chetvertkov**, V.A. Chetvertkova, M.B. Nurusheva, S.B. Nurushev, A.V. Ridiger, "*Helicity conservation hypothesis and pp-elastic scattering*," Physics of Particles and Nuclei **45**, 99-101 (2014).
4. E. Mayyas, I.J. Chetty, **M.A. Chetvertkov**, N. Wen, T. Neicu, T. Nurushev, L. Ren, M. Lu, H. Stricker, D. Pradhan, B. Movsas, M.A. Elshaikh, "*Evaluation of multiple image-based modalities for image-guided radiation therapy (IGRT) of prostate carcinoma: a prospective study*," Med Phys **40**, 041707 (2013).